Mon. Not. R. Astron. Soc. **394,** 1148–1166 (2009) doi:10.1111/j.1365-2966.2009.14388.x

Feeding versus feedback in NGC 4151 probed with Gemini NIFS – I. Excitation

T. Storchi-Bergmann,[1⋆] P. J. McGregor,[2] Rogemar A. Riffel,[1] R. Simões Lopes,[1] T. Beck[3] and M. Dopita[2]

[1]*Instituto de Física, Universidade Federal do Rio Grande do Sul, Av. Bento Gonçalves 9500, 91501-970 Porto Alegre RS, Brazil*
[2]*Research School of Astronomy and Astrophysics, Australian National University, Cotter Road, Weston Creek, ACT 2611, Australia*
[3]*Gemini Observatory and Space Telescope Science Institute, 3700 San Martin Dr., Baltimore, MD 21218, USA*

Accepted 2008 December 12. Received 2008 December 11; in original form 2008 July 11

ABSTRACT

We have used the Gemini Near-infrared Integral Field Spectrograph (NIFS) to map the emission-line intensity distributions and ratios in the narrow-line region (NLR) of the Seyfert galaxy NGC 4151 in the *Z, J, H* and *K* bands at a resolving power $\geq$5000, covering the inner $\approx$200 $\times$ 300 pc of the galaxy at a spatial resolution of $\approx$8 pc. We present intensity distributions in 14 emission lines, which show three distinct behaviours. (1) Most of the ionized gas intensity distributions are extended to $\approx$100 pc from the nucleus along the region covered by the known biconical outflow (position angle, PA = 60/240°, NE–SW), consistent with an origin in the outflow; while the recombination lines show intensity profiles which decrease with distance r from the nucleus as $I \propto r^{-1}$, most of the forbidden lines present a flat intensity profile ($I \propto r^0$) or even increasing with distance from the nucleus towards the border of the NLR. (2) The H_2 emission lines show completely distinct intensity distributions, which avoid the region of the bicone, extending from $\approx$10 to $\approx$60 pc from the nucleus approximately along the large-scale bar, almost perpendicular to the bicone axis. This morphology supports an origin for the H_2-emitting gas in the galaxy plane. (3) The coronal lines show a steep intensity profile, described by $I \propto r^{-2}$; the emission is clearly resolved only in the case of [Si VII], consistent with an origin in the inner NLR.

Using the line-ratio maps [Fe II] 1.644/1.257 and Pa β/Br γ, we obtain an average reddening of $E(B - V) \approx 0.5$ along the NLR and $E(B - V) \geq 1$ at the nucleus. Our line-ratio map [Fe II] 1.257 μm/[P II] 1.189 μm of the NLR of NGC 4151 is the first such map of an extragalactic source. Together with the [Fe II]/Paβ map, these line ratios correlate with the radio intensity distribution, mapping the effects of shocks produced by the radio jet on the NLR. These shocks probably release the Fe locked in grains and produce an enhancement of the [Fe II] emission at $\approx$1 arcsec from the nucleus. At these regions, we obtain electron densities $N_e \approx 4000\,cm^{-3}$ and temperatures $T_e \approx 15\,000$ K for the [Fe II]-emitting gas. For the H_2-emitting gas, we obtain much lower temperatures of $T_{exc} \approx 2100$ K and conclude that the gas is in thermal equilibrium. The heating necessary to excite the molecule may be due to X-rays escaping perpendicular to the cone (through the nuclear torus, if there is one) or to shocks probably produced by the accretion flow previously observed along the large-scale bar.

The distinct intensity distributions and physical properties of the ionized and molecular gas, as well as their locations, the former along the outflowing cone, and the latter in the galaxy plane surrounding the nucleus, suggest that the H_2-emitting gas traces the active galactic nuclei *feeding*, while the ionized gas traces its *feedback*.

Key words: galaxies: active – galaxies: individual: NGC 4151 – galaxies: ISM – galaxies: nuclei.

1 INTRODUCTION

NGC 4151 is the nearest and apparently brightest Seyfert 1 galaxy (or Seyfert 1.5, according to Osterbrock & Koski 1976), and thus

⋆E-mail: thaisa@ufrgs.br

harbours one of the best-studied active galactic nuclei (AGN) (Crenshaw & Kraemer 2007). As pointed out by Mundell et al. (1999), from old optical observations, NGC 4151 was believed to be a small spiral galaxy with major axis extending by ≈2.5 arcmin along position angle (PA) ≈130°. But this is just the inner part of the galaxy, comprising an oval distortion, or 'weak fat bar' (Mundell & Shone 1999), beyond which there is a much larger disc, weak in the optical, but bright in H I emission, with spiral arms extending up to 6 arcmin from the nucleus (Davies 1973). From the H I kinematics, it was concluded that the galaxy has a small inclination of $i \approx 21°$, and a major axis PA ≈ 22° (Davies 1973; Pedlar et al. 1992; Mundell et al. 1999; Das et al. 2005). Its radial velocity is $cz = 997\,\mathrm{km\,s^{-1}}$ (Pedlar et al. 1992), the Hubble type is (R')SAB(rs)ab, and we will adopt in this paper a distance of 13.3 Mpc, corresponding to a scale at the galaxy of 65 pc arcsec^{-1} (Mundell et al. 2003).

In radio continuum observations, NGC 4151 shows a linear structure comprising several knots elongated over ∼3.5 arcsec along PA ≈ 77°, which is embedded in a diffuse emission extending over ∼10.5 arcsec (Pedlar et al. 1993; Mundell et al. 1995). More recent high-resolution radio images (Mundell et al. 2003) reveal a faint jet underlying the discrete components which seem to be shock-like features produced by interactions of the jet with gas clouds in the galaxy, as well as neutral gas absorption consistent with being due to an obscuring torus.

In the optical, the narrow-line region (NLR) of NGC 4151 has been found to have a biconical morphology (both in [O III]λ5007 and in Hα emission lines), with the line of sight outside but close to the edge of the cones (Evans et al. 1993; Hutchings et al. 1998). The projected opening angle of the cones is ∼75°, and the projected axis is oriented along PA ∼ 60/240°. Optical spectroscopy reveals outflows along the cones, with the approaching side to the SW (Evans et al. 1993; Mediavilla & Arribas 1995). The outflows have been modelled in a number of studies (e.g. Hutchings et al. 1999; Crenshaw et al. 2000; Das et al. 2005), in which it is also argued that the AGN should be the primary ionization source of the bicone as no clear correlation with the radio jet is observed. The radio jet may be, nevertheless, associated with high-velocity clouds observed in the NLR (Winge et al. 1997).

Combining X-ray, UV and optical spectra, Kraemer et al. (2005, 2006) and Crenshaw & Kraemer (2007) were able to characterize outflows estimated to be at only ∼0.1 pc from the nucleus, obtaining a high mass outflow rate ($\sim 0.16\,\mathrm{M_{\odot}\,yr^{-1}}$) which is about 10 times the accretion rate necessary to feed the AGN in NGC 4151. They suggest that this outflow originates in an accretion disc wind.

In the near-infrared, Thompson (1995) obtained spectra from 0.87 to 2.5 μm, and concluded that, from the high emission-line ratios of [Fe II]/H I, the majority of the Fe should be in gaseous form, thus implying grain destruction to release a significant fraction of the iron usually tied up in dust. He obtained an electron temperature $T_\mathrm{e} \approx 10^4$ K and density $N_\mathrm{e} \approx 10^4\,\mathrm{cm^{-3}}$ for the region emitting [Fe II] lines. Long-slit *J*-band observations of the kinematics of the [Fe II]λ1.2570 μm and Paβ emission lines showed similar velocity structure to that observed in [O III] (Knop et al. 1996), which was later confirmed with two-dimensional (2D) Integral Field Unit (IFU) observations (Turner et al. 2002). This similarity supports the same origin for [O III] and [Fe II] emission, namely photoionization by the AGN in the NLR. Nevertheless, broadening of the [Fe II] emission relative to Paβ, which is observed along the NLR (Knop et al. 1996), suggests additional processes contributing to the [Fe II] emission, such as shocks from an AGN wind or jet.

Despite being a well-studied galaxy (Ulrich 2000), the dynamics and excitation of the NLR, as well as the role of the radio jet, are not yet fully understood. In the present paper, we use the Gemini Near-infrared Integral Field Spectrograph (NIFS) equipped with the adaptive optics module ALTitude-conjugate Adaptive optics for the InfraRed – to map the NLR gas distribution and excitation in the inner ≈200 × 400 pc, at a spatial resolution of ≈7 pc at the galaxy. The data cover the wavelength range 0.95–2.51 μm at a spectral resolving power over 5000. In a companion paper (Simões Lopes et al. in preparation), we use these data to obtain the gas kinematics and present emission-line channel maps of the NLR obtained by slicing the strongest emission-line profiles in velocity bins of 60 km s^{-1}.

The present paper is organized as follows. In Section 2, we describe the observations and reductions. In Section 3, we present the results, which include flux measurements of 55 emission lines and 14 intensity distribution maps as well as line-ratio maps. In Section 4, we derive physical parameters for the NLR and discuss the origin of the [Fe II] and H_2 emission, and in Section 5 we present our conclusions.

2 OBSERVATIONS AND REDUCTIONS

2D spectroscopic data were obtained on the Gemini North telescope with the NIFS instrument (McGregor et al. 2003) operating with the ALTAIR adaptive optics module on the nights of 2006 December 12, 13 and 16 UT. ALTAIR was used in its Natural Guide Star mode with optical light from the nucleus of NGC 4151 feeding the adaptive optics wave front sensor. The uncorrected seeing full width at half-maximum (FWHM), as reported by ALTAIR, was generally in the range 0.6–0.9 arcsec, measured in the *V* band, but reached 1.2 arcsec on some occasions. The observations covered the standard *Z*, *J*, *H* and *K* spectral bands at two-pixel resolving powers of 4990, 6040, 5290 and 5290, respectively. This resulted in wavelength coverage of 0.94–1.16, 1.14–1.36, 1.49–1.81 and 1.99–2.42 μm, respectively. Additional spectra were obtained at the K_long setting of the *K* grating. This covers the wavelength range 2.09–2.51 μm, which includes the H_2 Q-branch.

NIFS has a square field of view of ≈3.0 × 3.0 arcsec^2, divided into 29 slitlets each 0.103 arcsec wide with a spatial sampling of 0.042 arcsec along each slitlet. The FWHM of the spatial profile of a star is 0.12 ± 0.02 arcsec at the *H*, *K* and K_long bands, corresponding to ≈8 pc at the galaxy, while at the *J* and *Z* bands it is larger, 0.16 ± 02 arcsec, corresponding to ≈10 pc at the galaxy. This is dominated by the 0.1 arcsec slitlet width across the slitlets and by instrumental aberrations along the slitlets. But, we have verified an increasing strength of the uncorrected seeing halo towards shorter wavelengths, which degrades the image quality. In order to gauge the performance of our data in terms of image quality, we have measured the flux in a 0.2 arcsec diameter circular aperture and in a 1.5 arcsec diameter circular aperture for each of the telluric standard stars. The resulting ratio between the flux in the smaller aperture to the one in the larger aperture is 0.19 for the *Z* band, 0.27 for the *J* band, 0.30 for the *H* band, 0.47 for the *K* band and 0.43 for the K_long band.

Fig. 9 shows the spatial profiles of a star in different bands, as compared with the spatial profiles in the galactic continuum in the *Z, J, K* and K_long bands. It can be argued that, as the observations were obtained using the galaxy nucleus as a guide star, the real point spread function (PSF) should be that derived from the spatial profile of the nuclear source, instead of the stellar profile. It can be seen that in the *K* band, the FWHM of the nuclear source profile is almost indistinguishable from that of the star, while in the K_long band it is

0.04 arcsec larger thus 0.16 arcsec. In the *J* band, the FWHM of the nuclear source is smaller that of the stellar profile, thus we adopt for the PSF the larger stellar value of 0.16 ± 02 arcsec, while in the *Z* band the FWHM of the nuclear source is significantly larger than that of the star, 0.24 arcsec. In the *H* band, the FWHM of the nuclear source profile is 0.15 ± 0.02 arcsec. Thus, a representative value for the FWHM of the PSF in the *J, H, K* and K_{long} bands is 0.14 ± 0.02 arcsec, corresponding to a spatial resolution at the galaxy of 9 ± 1.3 pc. In the *Z* band, the resolution is poorer, corresponding to 15 ± 1.3 pc at the galaxy.

The instrument was set to a PA of 345° to align the slitlets approximately perpendicular to the axis of the radio jet in NGC 4151 (Mundell et al. 2003). This results in coarser spatial sampling along the jet and finer spatial sampling across it. The *Z*, *J*, *H* and *K* observations covered three adjacent NIFS fields centred on the NGC 4151 nucleus and offset by ± 2.5 arcsec along PA 75°. The resulting field of view is 8.0 × 3.0 arcsec^2. Only a single NIFS field was obtained at the K_{long} grating setting due to the limited extent of the H_2 emission. This was centred on the nucleus at the same PA as the other observations.

Each data set was recorded as a sequence of two 90 s exposures at each of the three field positions on NGC 4151 followed by two 90 s sky exposures. The nucleus did not saturate in this time. The sky positions were displaced by ≈ ±75 arcsec from NGC 4151 along PA = 75° and dithered by ±0.2 arcsec. This sequence was repeated three times and concluded with a fourth object set. It resulted in eight object frames at each field position and six offset sky frames for each grating setting. An arc spectrum was obtained along with each data set, and the spectra of the nearby *Hipparcos* stars HIP 56324 (A3V) and/or HIP 61471 (A0V) were obtained before and/or after the NGC 4151 observations to provide telluric correction. The *Hipparcos* star observations were also used for flux calibration.

The data reduction was accomplished using tasks contained in the NIFS package, which is part of the GEMINI IRAF package, as well as generic IRAF tasks. The reduction procedure first applied a linearity correction and then subtracted a median-combined sky frame, multiplied by a flat-field frame, and cut each object frame into 29 sub-images, one for each NIFS slitlet. Bad pixels identified in the flat-field and dark frames were then removed by interpolation. A coordinate transformation was then applied to each 2D sub-image to linearize the wavelength and spatial scales. These were derived from the arc exposure and exposures of the flat-field lamp with a Ronchi grating aligned perpendicular to the NIFS slitlets, respectively. The transformed 2D images were then stacked into a 3D data cube with two spatial and one spectral dimension. The data cubes for each object exposure were then collapsed in the spectral direction to produce a continuum image of the sky, and the centroid of the NGC 4151 nucleus was measured. The individual data cubes were then recentred to remove tracking drift and combined using the IRAF IMCOMBINE task. Each spectrum in the combined data cube was then corrected for telluric absorption based on the spectrum of the A-type *Hipparcos* star after intrinsic hydrogen absorption had been removed by Gaussian fitting. The spectra were then flux-calibrated by reference to the telluric-corrected spectrum of the *Hipparcos* star, which was assumed to have a blackbody shape over the wavelength range of each near-infrared spectral band and an average absolute flux density defined by the appropriate Two Micron All Sky Survey *J*, *H* or *K* broad-band magnitude. The total signal of the *Hipparcos* star was measured in a 1.5 arcsec diameter aperture and thus includes as much of the uncorrect adaptive-optics halo light from the star as practical to measure in our 3.0 × 3.0 arcsec^2 field. As such, the flux calibration applies to *detected* light per spatial pixel: no correction is attempted to the total flux in the adaptive-optics-corrected PSF.

Inspection of individual spectra of telluric stars in the *Z* and *J* bands showed flux variations of 18 per cent in data obtained just before and after the galaxy observations. These fluctuations indicate that the night of 2006 December 13, when these observations were made, had variable seeing, as there is no report of the presence of clouds during the night. During the previous night, when the *H*- and *K*-band observations were made, and on December 16, when the K_{long} observations were made, the seeing was stable. As a result, the flux-calibrated spectra of the galaxy show a flux excess of ≈17 per cent when we compare the red end of the *J*-band spectra to the blue end of the H spectra. We have thus re-calibrated the *Z*- and *J*-band fluxes dividing them by a factor of 1.17, in order to have consistent data over all spectral bands.

The final data cubes contain 2250 spectra per band, with each spectrum corresponding to a spatial coverage of 6.6 × 2.7 pc^2 at the galaxy. Although the total field covered in the *Z*, *J*, *H* and *K* observations is 3 × 8 arcsec^2, most of the line emission, which is the subject of the present study, is concentrated within the inner 3 × 5 arcsec^2, corresponding to a region of dimensions 192 × 320 pc at the galaxy.

3 RESULTS

In the top panel of Fig. 1, we present a *K*-band image of the central 60 × 60 arcsec^2 of NGC 4151, obtained with the William Herschel Telescope (WHT), where the bar can be observed at PA = 130°. We note that the position of the major axis of the galaxy (22°) is almost perpendicular to the bar. The central rectangle shows the field of view covered by the NIFS observations. In the bottom panel, we present an image obtained from the NIFS observations integrating the flux of the [Fe II] 1.6440 μm emission line, where we have marked the positions of representative spectra shown in Figs 2 and 3.

The spectra shown in Fig. 2 cover the *Z* and *J* bands, while those in Fig. 3 cover the *H* and *K* bands. From top to bottom, we show spectra from locations approximately at 1.4 and 0.7 arcsec E of the nucleus (PA = 75°), from the nucleus, from 0.7 arcsec W of the nucleus (PA = 255°) and from 0.7 arcsec SE of the nucleus (PA = 120°), respectively. The emission lines identified in the spectra are listed in Table 1, together with the corresponding fluxes at the nucleus, at 0.9 arcsec SW (0.2 arcsec to the right of Position D in Fig. 1, where there is a peak in the [Fe II] emission), 0.7 arcsec SE of the nucleus (Position E in Fig. 1, where there is a peak in the H_2 emission) and 0.7 arcsec E (Position B in Fig. 1), for an aperture of 0.31 × 0.31 arcsec (obtained by binning 3 pixel along the *x*-axis and 7 pixel along the *y*-axis).

Figs 2 and 3 show that the nuclear continuum (panel C) is very red, while the continuum from extra-nuclear regions is blue. An analysis of this continuum, and the constraints which can be derived for the structure producing it – possibly a dusty torus – will be presented in a forthcoming paper (Riffel et al. in preparation). The nuclear spectrum shows broad H I and He I emission lines, and a deep absorption which is clearly observed on top of the broad profiles in the nuclear He I 1.08332 μm, Brγ and He I 2.05869 μm emission lines. It can also be observed that there is no H_2 emission at the nucleus and that the coronal lines of [Ca VIII] and [Si VII] seem to be extended. The [P II] 1.1886 μm emission line is also extended and can be observed up to 1.4 arcsec E of the nucleus. This line was first reported in an extragalactic source by Oliva et al. (2001),

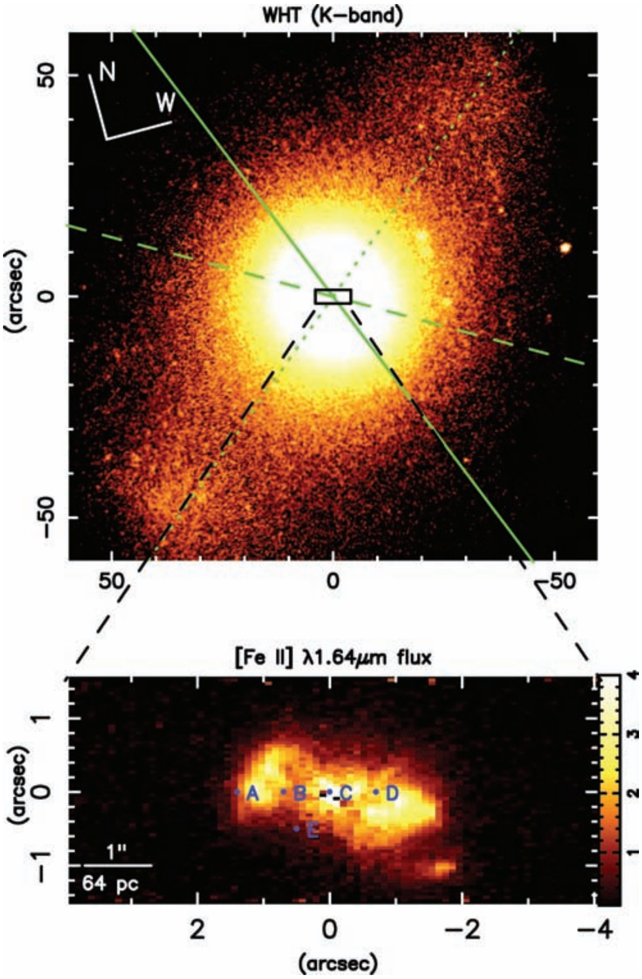

Figure 1. Top: *K*-band image of the central 60 × 60 arcsec^2 of NGC 4151 obtained with WHT. The image has been rotated to the same orientation of the NIFS frames. The continuous line shows the orientation of the major axis of the galaxy, the dashed line shows the orientation of the bicone and the dot–dashed line shows the orientation of the bar (visible in the image). The rectangle shows the region covered by the NIFS observations. Bottom: image obtained from the NIFS frames integrating in the [Fe II]λ 1.644 μm emission line; the letters identify locations corresponding to the spectra shown in Figs 2 and 3.

and since then it was observed in the nuclear spectrum of less than 15 galaxies, including NGC 4151 (Riffel, Rodríguez-Ardila & Pastoriza 2006a). Combined with [Fe II]1.2570 μm, the [P II] line is a powerful diagnostic of the origin of the [Fe II] emission in galaxies (Oliva et al. 2001; Jackson & Beswick 2007). In the present paper, we provide the first 2D map of an extragalactic source in this emission line.

The profiles of most of the emission lines vary according to the location in the NLR, and an illustration of this variation is shown in Fig. 4, where we present a sequence of selected emission-line profiles, from different locations along the bicone (PA = 60°). A vertical dashed line shows the adopted systemic velocity of 997 km s^{-1} (Pedlar et al. 1992). The same flux scale is kept for each emission line in Fig. 4, so that the flux variation can also be observed as a function of distance from the nucleus. The scale nevertheless varies for the different emission lines. It can be observed that the centre of the emission lines drifts from blueshifts observed to the SW of the nucleus to redshifts observed to the NE of the nucleus. In some locations – e.g. at 0.8 arcsec SW of the nucleus in Fig. 4 – many emission lines are clearly double-peaked, while in other locations the profiles are asymmetric suggesting the presence also of two components, although unresolved. The blueshifted absorption in the He I 1.08332 μm emission-line profile is observed at −468 km s^{-1} relative to the systemic velocity (more details will be given in Simões Lopes et al. in preparation). A similar absorption (with similar blueshift) is observed in Brγ and in the He I 2.0587 μm lines. The absorption in both He I lines reaches below the interpolated continuum indicating that the absorber covers much of the continuum source and the BLR clouds. To our knowledge, these absorption features have not been seen in previous near-infrared spectra, such as the one obtained by Osterbrock, Shaw & Veilleux (1990) in 1988 or by Thompson (1995) in 1993. More recently, Riffel et al. (2006a) also fail to detect this absorption. Nevertheless, absorptions of similar widths and blueshifts have been observed in the UV and optical. Kraemer et al. (2001) report absorptions at a velocity −490 km s^{-1} with respect to systemic in *Hubble Space Telescope* (*HST*) UV spectra of the NLR of NGC 4151, which had been previously identified as due to components called *D* and *E* in a previous study by Weymann et al. (1997), while Hutchings et al. (2002) report an absorption due to He I λ3889 Å at −460 km s^{-1}. The absorptions we see in the near-IR are probably related to these UV and optical absorptions seen in *HST* spectra. Its detection in our spectra is aided by the high spatial resolution of the NIFS data, which minimizes NLR contamination of the nuclear spectrum.

3.1 Emission-line intensity distributions

2D maps of the emission-line intensities have been obtained by integrating the flux under the line profiles, after subtraction of the contribution of the underlying continuum, determined as the average between two spectral windows adjacent to the emission lines. In the case of the H and He lines, which have broad components at the nucleus, the adjacent continua fall on top of the broad lines, and thus the resulting flux is essentially from the narrow component. Nevertheless, as the broad-line profiles are not symmetric (e.g. Paβ profile in the middle panel of Fig. 2), the subtraction is not always perfect and the nuclear fluxes in these lines may have some residual broad-line flux.

The intensity maps for the main extended emission lines from the *Z* and *J* bands, namely [S III] 0.9533 μm, [S VIII] 0.9915 μm, He II 1.0126 μm, [S II] 1.029,1.032,1.034,1.037 μm, He I 1.0833, [P II] 1.1886 μm, [S IX] 1.2523 μm and [Fe II] 1.2570 μm are shown in Fig. 5. Along the *y*-axis, we show the whole extent of the frames (3 arcsec), while along the *x*-axis we show only the region with measurable flux in at least one of the emission lines, comprising the inner 4.6 arcsec. We have overplotted on the He I flux map the contours (in blue) of a radio λ21 cm image from Mundell et al. (1995), obtained with Multi-Element Radio-linked interferometer (MERLIN). These contours have been aligned to the intensity maps under the assumption that component C_4 of the radio image is aligned with the peak of our *K*-band continuum map. Radio component C_4 is claimed to contain the active nucleus. We assume that the *K*-band continuum peak also contains the nucleus. The continuous line in the top-left panel shows the orientation of the major axis of the galaxy at PA = 22° (Pedlar et al. 1992), while the dashed line shows the orientation of the [O III] bicone at PA = 60/240°, and the dot–dashed line shows the orientation of the bar, at PA = 130° (Mundell & Shone 1999). The [P II] flux map, shown in the second panel (from top to bottom) to the right-hand side of Fig. 5, is the

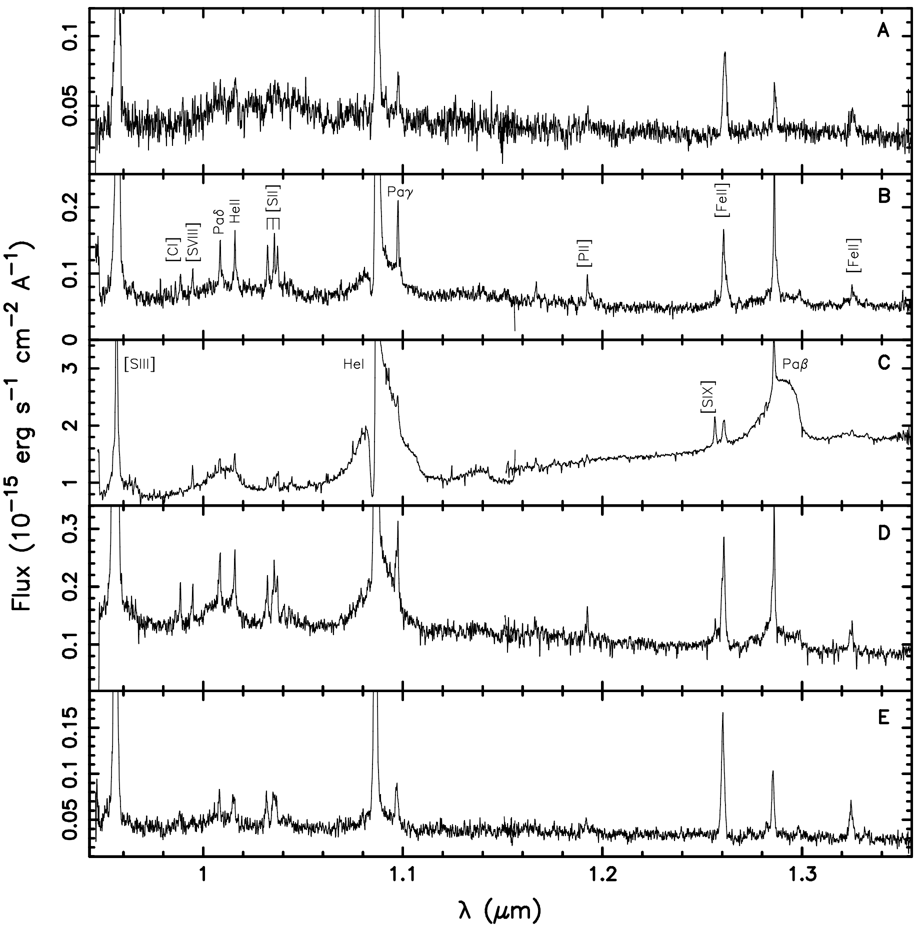

Figure 2. Sample of spectra in the *Z* and *J* bands, with the corresponding locations identified in the NIFS [Fe II] image shown in Fig. 1. From top to bottom: (A) spectrum from a location 1.4 arcsec E of the nucleus (PA = 75°); (B) spectrum from 0.7 arcsec E of the nucleus (PA=75°); (C) spectrum from the nucleus; (D) spectrum from 0.7 arcsec W of the nucleus (PA=255°); (E) spectrum from 0.7 arcsec SE of the nucleus (PA = 120°), where there is a maximum in the H_2 emission (Fig. 6).

first 2D map in this line ever obtained for an extragalactic source (as pointed out in the previous section). The resolution achieved in the images can be judged by a comparison with telluric star images, shown as insets in Fig. 5: the image of a star in the *Z* band is shown in the [S III] panel, while that in the *J* band is shown in the [P II] panel, with peak intensity normalized to that of the galaxy in the emission line of the corresponding panel.

In Fig. 6, we show the intensity maps for additional emission lines observed in the *J, H* and *K* bands, namely Pa β, [Fe II] 1.6440 μm, H_2 2.1218 μm, Br γ, [Ca VIII] 2.3220 μm and [Si VII] 2.4833 μm. We have overplotted (in blue) on the [Fe II] map the contours of the [O III] emission-line map.

From Figs 5 and 6, it can be observed that the light distribution varies for different emission lines. For the coronal lines [S VIII], [S IX] and [Ca VIII], the light distribution is compact and not clearly resolved, while the coronal [Si VII] emission distribution is more extended, being aligned with the bicone to the SW and with the radio jet to the NE.

Except for H_2, the other emission lines show much stronger extended emission, reaching at least 4 arcsec along the bicone and 2 arcsec in the perpendicular direction, corresponding to projected distances at the galaxy of 256 and 128 pc, respectively. The intensity distributions are somewhat brighter and more extended to the SW (the near side of the bicone) than to the NE (the far side).

The [O III] image, whose contours are overplotted on the [Fe II] intensity distribution in Fig. 6, has a 'knotty' appearance, similar to what is observed in our [Fe II] map, with some knots coinciding in both maps. Nevertheless, a detailed comparison shows that the decrease in emission just outside the nucleus and increase again in two opposite regions at about 1 arcsec from the nucleus along the bicone observed in the [Fe II] maps are not observed in the [O III] map, which shows emission in 'curved strands' all the way along the bicone (Hutchings et al. 1998).

A completely different light distribution is observed in the H_2 flux map (bottom-left panel of Fig. 6): instead of being elongated along the bicone axis, it is elongated almost perpendicular to it. There is almost no H_2 emission within ≈0.3 arcsec from the nucleus; its flux being distributed in two structures resembling double arcs to the NW and SE, extending from ≈0.3 to ≈1 arcsec from the nucleus along the minor axis of the galaxy (PA = 112/292°), which is also approximately the orientation of the bar.

In order to look for a possible relation between the emission-line intensity distributions and the radio emission, we have overplotted the radio contours of the MERLIN radio image of Mundell et al. (1995) on the He I flux map (top-right panel of Fig. 5). While the radio intensity distribution is oriented horizontally in the figure, along PA = 75°, most intensity distributions are oriented instead along the [O III] bicone at PA = 60/240°. Thus, there seems not to

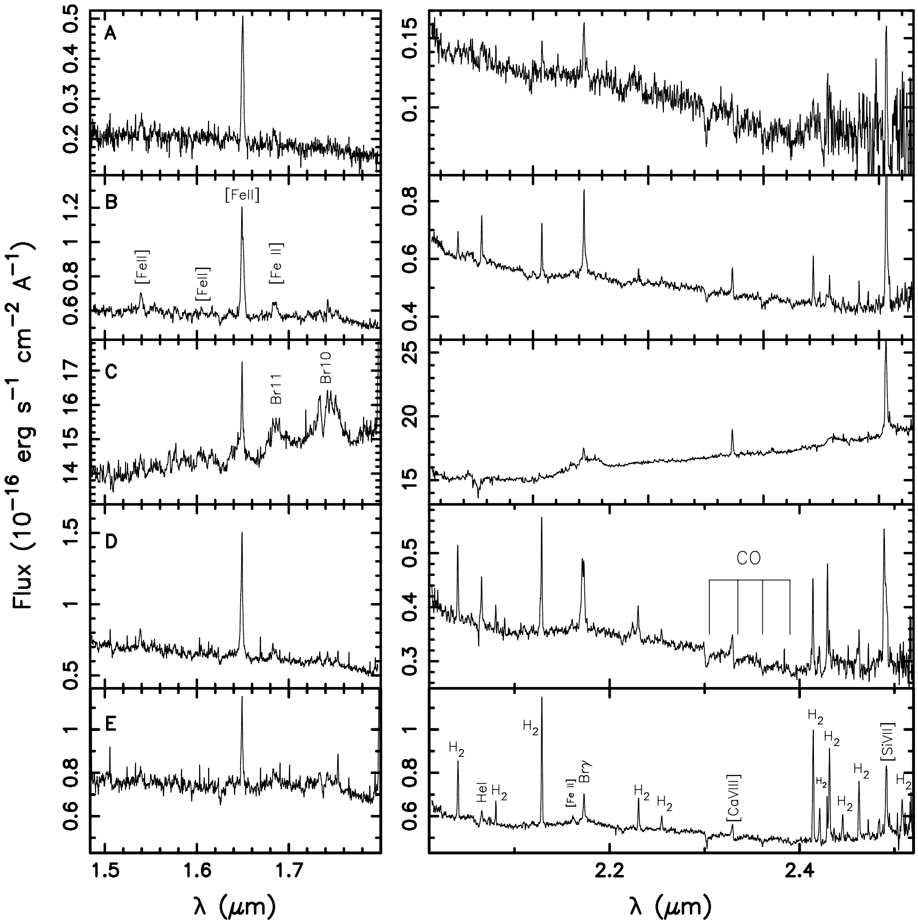

Figure 3. Sample of *H*- and *K*-band spectra, with the corresponding locations identified in the NIFS [Fe II] image shown in Fig. 1, and specified in the caption of Fig. 2.

be a strong association between the radio jet and the line emission. On the other hand, both the radio and line emission are stronger to the SW than to the NE, and a closer inspection shows that the radio component C_3 (the radio knot just W of the nucleus) seems to align well with a region of enhanced emission 0.4 arcsec W from the nucleus observed in the [Fe II] 1.6440 μm map.

3.2 Line-ratio maps

We have used the intensity maps to construct the line-ratio maps [S II]/[S III], [S III]/Paβ, [Fe II] 1.257/Paβ, [Fe II] 1.257/[P II], H_2 2.122/Brγ, [Fe II] 1.644/1.533, [Fe II] 1.644/1.257 and Br γ/Pa β, which are shown in Fig. 7. As pointed out above, at the nucleus (and within $\approx$0.2 arcsec from it), there may be some contribution from the broad-line component in Paβ and Brγ; thus the nuclear ratios involving these two lines may be affected by this component. Many of these line ratios are indicators of the gas excitation, thus the nuclear values should be used with caution.

The [S III]/Paβ line-ratio map has values of $\approx$4 at the nucleus, increasing outwards to $\approx$12 to the SW and $\approx$8 to the NE. There is thus a systematic difference in the values of this line ratio between the two sides of the bicone: higher ratios in the near side (SW) and lower ratios in the far side (NE). The [S II]/[S III] ratio map has the lowest values $<$0.1 at the nucleus, increasing outwards up to 0.2.

We have overplotted the contours of the MERLIN radio image on the line-ratio [Fe II]/Paβ map in order to look for a possible relation between the [Fe II] excitation and the radio emission. There is indeed a relation: both the [Fe II]/Paβ and [Fe II]/[P II] (Fig. 7) line ratios increase outwards, reaching maximum values at $\approx$1 arcsec SW, the location where the radio jet shows a 'flaring' in its distribution, and to the opposite side at $\approx$1 arcsec NE, the location of a radio hotspot. The [Fe II]/Paβ ratio increases from values $<$1 close to the nucleus up to $\approx$3 at the locations of the radio SW flare and NE hotspot, while [Fe II]/[P II] increases from values $\approx$4 to $\approx$8 at these same locations. The line-ratio [Fe II] 1.644/1.533, which is sensitive to the emitting gas density, shows values $<$4 within the inner 0.5 arcsec, increasing to $\approx$8–10 in the outermost regions.

The H_2/Brγ line-ratio distribution is a result of the H_2 intensity distribution, which shows low or zero fluxes at and close to the nucleus and higher values perpendicular to the bicone. The consequence is an increase in the line ratio from values $\leq$1 around the nucleus to $>$3 towards the borders of the H_2 emitting regions at $\approx$1 arcsec to the NW and SE of the nucleus. As in the case of Paβ, within 0.3 arcsec from the nucleus, the line ratios may be affected by the broad component of the Brγ line, and thus should not be used as an indicator of the gas excitation.

The line ratios [Fe II] 1.644/1.257 and Br γ/Pa β are shown in the bottom panels of Fig. 7. These line ratios can be, in principle, used for estimates of the reddening along the NLR, although the wavelength baseline is small, mainly for the [Fe II] ratio. The highest values are observed at the nucleus, for both ratios. In the [Fe II] 1.644/1.257 ratio map, there is a hint of a structure resembling

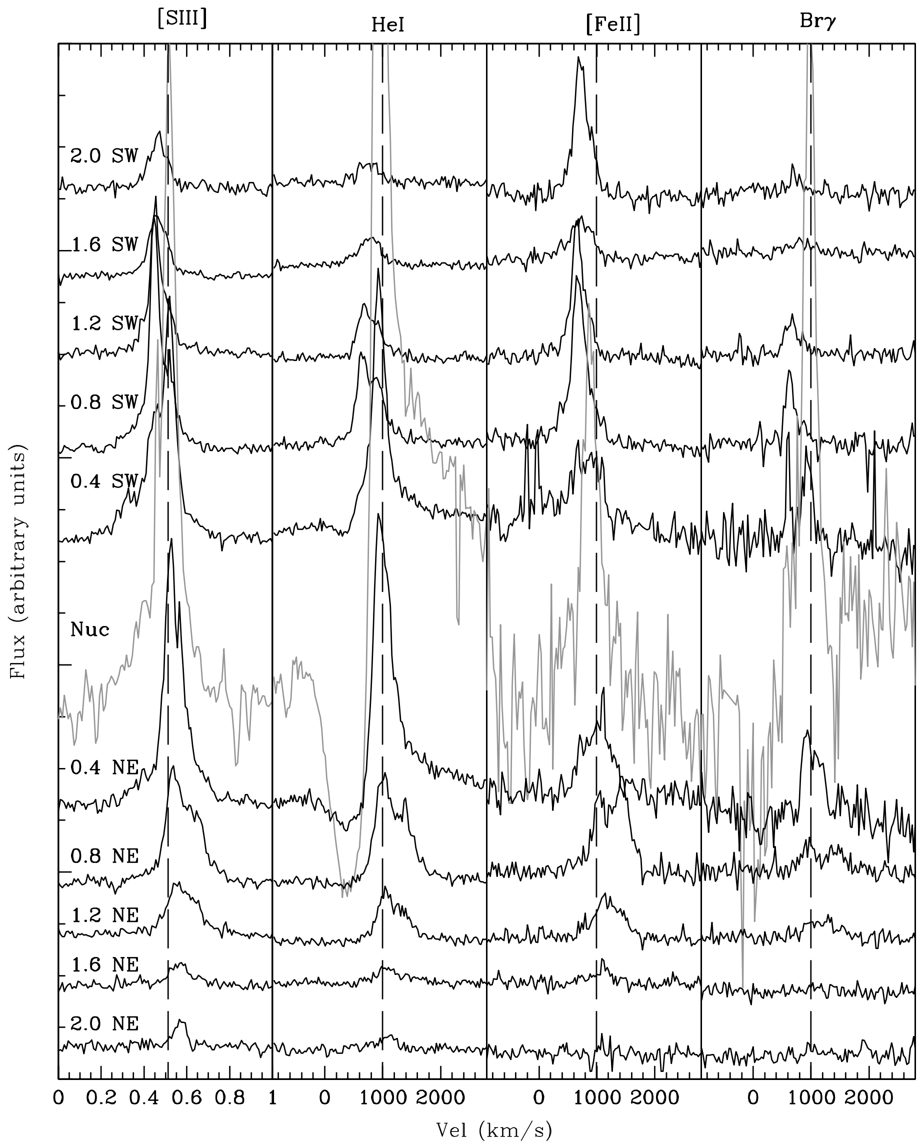

Figure 4. Sample of profiles of the [S III] 0.9533 μm, He I 1.0833 μm, [Fe II] 1.2570 μm and Brγ 2.1661 μm emission lines, from spectra extracted along the bicone axis (PA = 60°), at the locations relative to the nucleus indicated in the figure. The same flux scale is kept at all locations for each emission line, but varies from line to line.

the curved strands observed in the [O III] image (whose contours are overplotted on this map) in which the highest ratios seem to be observed in the regions of lowest [O III] fluxes. Data with better spatial resolution and higher signal-to-noise ratio would be necessary in order to confirm this result.

4 DISCUSSION

4.1 Ionized gas distribution

The intensity distributions in the emission lines of the ionized gas (with the exception of the [S VIII], [S IX], [Ca VIII] and [S VII] coronal lines) resemble that of the optical [OIII] emission line, suggesting a similar origin, namely emission from ionized gas outflowing along the walls of a hollow bicone centred at the nucleus and oriented along PA = 60/240° (Hutchings et al. 1999; Crenshaw et al. 2000; Das et al. 2005). Nevertheless, as pointed out by Kraemer, Schmitt & Crenshaw (2008), these intensity distributions do not clearly delineate a bicone, showing also extended emission perpendicular to the axis of the bicone in the vicinity of the nucleus. In other words, there is line emission beyond the presumed walls of the bicone close to the nucleus, indicating some escape of radiation in the perpendicular direction.

The fact that the light distributions are more extended and somewhat brighter to the SW than to the NE can be understood as due to the SW cone being directed towards us, and we are looking inside the cone, where we are observing the gas most exposed to the nuclear radiation field. To the NE we are observing the emission through both the wall of the far cone and the galactic plane (see discussion below and in Simões Lopes et al. in preparation).

Radial profiles of the NLR emission have been obtained by averaging the line flux within conical regions having an opening angle of 40° centred on the nucleus and oriented along the bicone axis at PA = 60° and 240°. These radial profiles are shown in Fig. 8. Profiles of [O II] 3727Å and [O III] 5007Å are also plotted from data presented by Kraemer et al. (2008). All profiles decline steeply

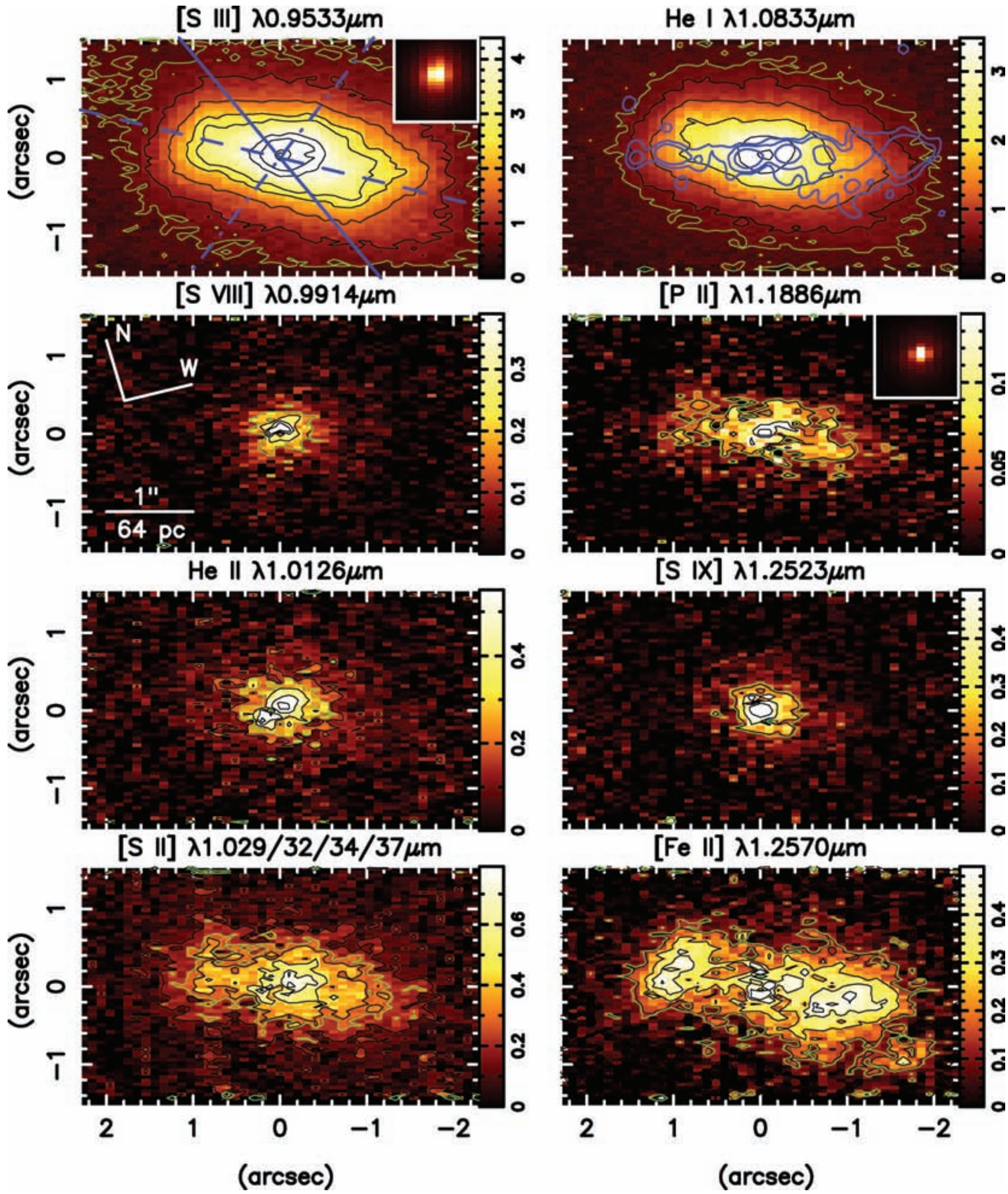

Figure 5. Intensity maps of emission lines from the *Z* and *J* bands, obtained by integrating the flux under the line profiles after subtraction of the continuum. The green contours correspond to three times the background noise (3σ). The blue contours are from the radio MERLIN image of Mundell et al. (1995). The dashed line on the top-left panel shows the orientation of the bicone, the continuous line shows the galaxy major axis and the dot–dashed line shows the orientation of the large-scale bar. The insets show images of telluric stars in the *Z* band (in the [S III] panel) and *J* band (in the [P II] panel) with peak intensity normalized to that of the galaxy in the emission line of the corresponding panel. Flux units are 10^{-15} erg cm^{-2} s^{-1} spaxel^{-1}.

beyond the edge of the bright inner NLR at radii between 1 and 2 arcsec. Among the near-IR profiles, the strongest features are those of [S III] 0.9533 μm (green crosses) and He I 1.083 μm (black open circles).

Three distinct behaviours can be observed for the radial profiles in Fig. 8. The first is observed for [S III] 0.9533 μm (green crosses) and the recombination lines of He I 1.083 μm (black open circles), Pa β (black crosses) and He II 1.013 μm (dark blue crosses). Their intensity profiles decrease monotonically with distance from the nucleus, showing a dependence on the radial distance of $\approx I \propto r^{-1}$, as illustrated by the black dashed lines in Fig. 8. In order to understand the behaviour of the lines, it would be necessary to construct models to try to constrain the physical parameters which lead to line emission, which is beyond the scope of the present study. A preliminary comparison of the radial profiles with models by Groves, Dopita & Sutherland (2004a) and Groves, Dopita & Sutherland (2004b) suggests that profiles such as the above are reproduced by models including dusty radiation-pressure-dominated clouds. Dust-free models for the NLR result in radial profiles for the Pa β, He I and He II emission lines which are steeper than those observed.

A distinct behaviour is observed in the [Fe II] radial profile (red crosses in Fig. 8), which is enhanced at radii around ~1 arcsec due

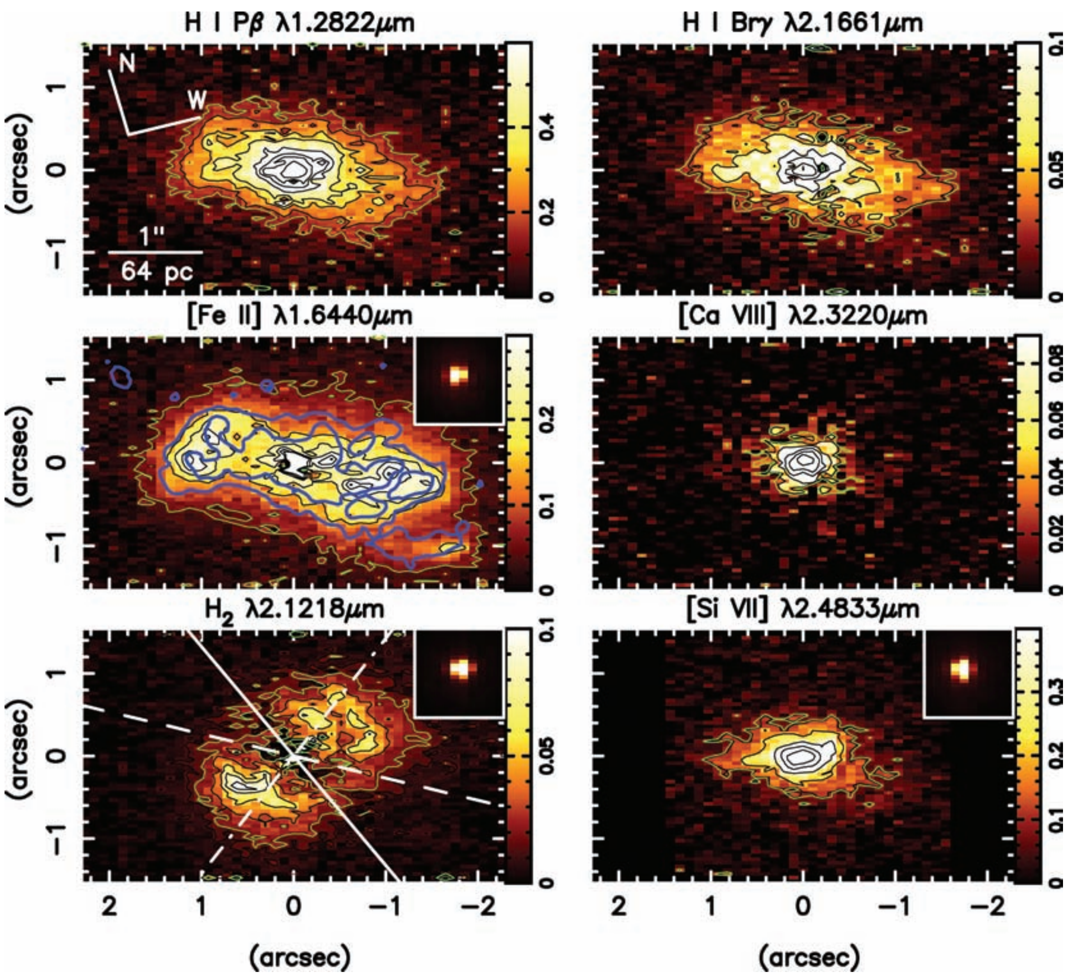

Figure 6. Intensity maps of emission lines from the *J, H* and *K* bands, represented as in Fig. 5. Blue contours overplotted on the [Fe II]λ 1.644 μm map are from the [O III] image of Hutchings et al. (1998). The insets show images of telluric stars in the *H* band (in the [Fe II] panel), *K* band (in the H_2 panel) and in the K_{long} band (in the [Si VII] panel), normalized to the peak intensity of the galaxy in the emission line of the corresponding panel.

to the emission clumps that are apparent in Fig. 6. This could be explained by excess gas-phase abundance caused by shocks produced by the radio jet that has destroyed dust grains and released Fe. Support for this interpretation is given by the correlation between by the [Fe II]/[P II] ratio and the radio jet. In Simões Lopes et al. (in preparation), we also find a spatial correlation between the radio jet and the [Fe II] kinematics. The behaviour of [Fe II] emission can also be partly due to the fact that [Fe II] is produced in partially ionized regions beyond the main hydrogen ionization front in NLR clouds. Progressive absorption of FUV photons near the hydrogen ionization edge by absorbing clouds located between the central black hole and the NLR hardens the photoionizing spectrum. It is possible that the NLR has become optically thick to hydrogen-ionizing FUV radiation in its outer parts while it remains optically thin to X-rays from the AGN. In these circumstances, the outer NLR clouds could develop extensive partially ionized regions that emit relatively more [Fe II] than P β.

[O II], [O III] and [S II] (black asterisks, black filled circles and red circles, respectively) show a similar behaviour to that of [Fe II], which can be approximately described as $I \propto r^0$.

A third behaviour is observed in the coronal lines, which we will discuss now.

4.2 Coronal gas distribution

Fig. 8 shows that the all the coronal lines (light blue and magenta symbols) decline more steeply with radius than the recombination lines. In fact, they are well represented by an $I \propto R^{-2}$ intensity decline, similar to that observed for the star radial profiles (shown as dashed blue and red lines in Fig. 8). The [Ca VIII] feature (light blue circles in Fig. 8) declines even more steeply at small radii.

In order to verify if the coronal emission is resolved and quantify its extent, we have constructed azimuthal averages within circular radial annuli of the light distribution in each coronal line and have normalized the profile to unity at the peak. The resulting spatial profiles are shown in Fig. 9 together with those in the galaxy continuum and telluric standard stars. In the top panel, we compare the profiles of the [S VIII] λ 0.991 μm and [S IX] λ 1.252 μm coronal lines with those in the continuum and telluric star in the *Z* and *J* bands, respectively. In the bottom panel, we compare the profiles of the [Ca VIII] λ2.322 μm and [Si VII] λ2.483 μm coronal lines with those in the continuum and telluric star in the *K* and K_{long} bands, respectively. As discussed in Section 2, if we assume that the PSF is given by the profile in the galaxy continuum, instead of the stellar profiles (except for the *J* band, where we adopt the broader stellar profile),

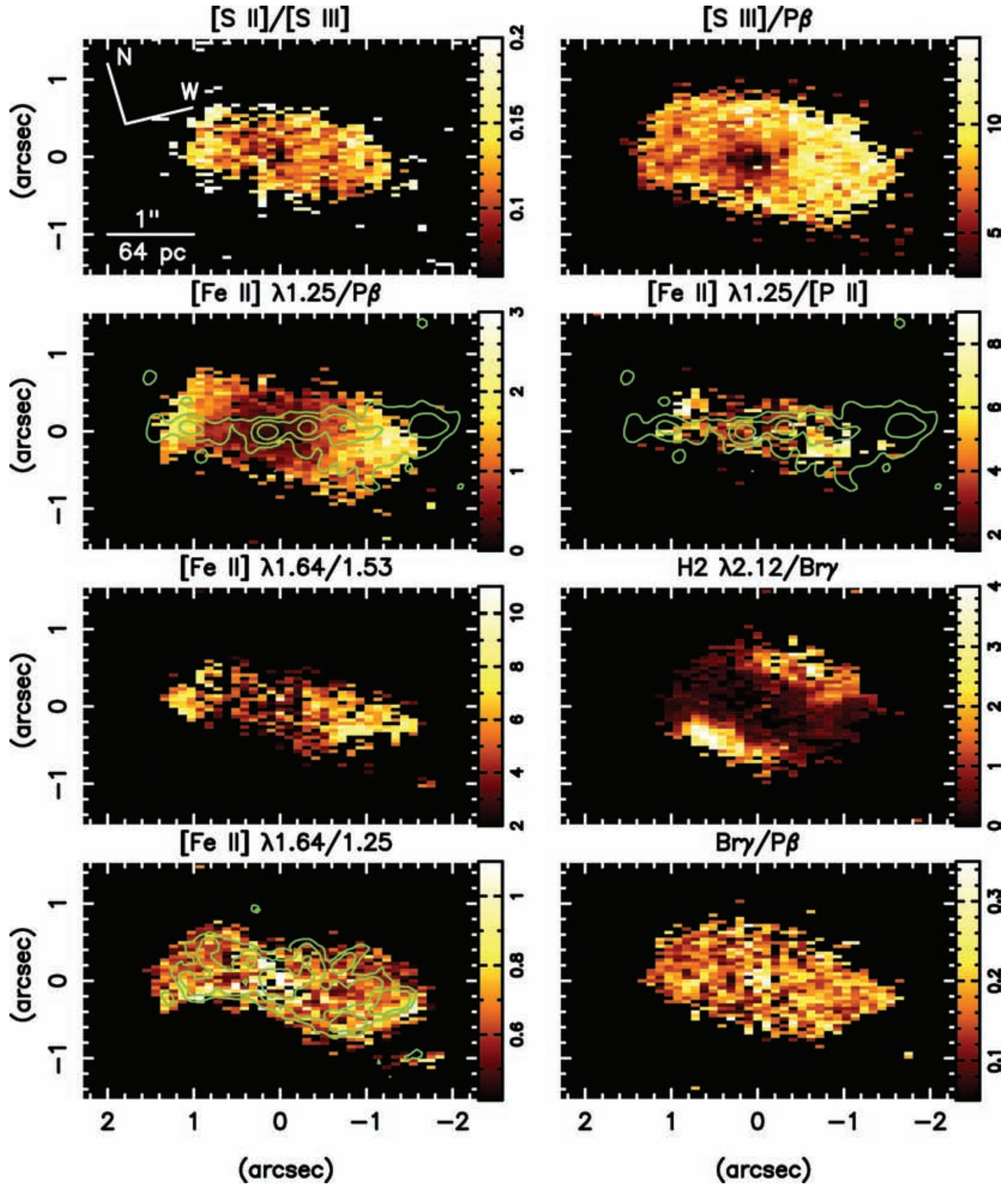

Figure 7. Line-ratio maps, where the green contours overplotted on the [Fe II]/Pa β and [Fe II]/[P II] maps, are from the radio MERLIN image of Mundell et al. (1995), while the ones overplotted on the [Fe II]1.644/1.257 map are from the [O III] image of Hutchings et al. (1998).

one concludes that none of the coronal lines is strongly resolved, except for [Si VII], which is somewhat extended along the bi-cone axis, what can be seen already in Fig. 6. [Ca VIII] may be slightly more extended than the nuclear continuum, but higher spatial resolution and better sampled data, possibly with better signal-to-noise ratio, would be required to confirm this given that the NIFS spaxels have a size of 0.1 arcsec in one direction.

The fact that the light distributions in [S IX] and possibly [Ca VIII] coronal lines are extended, support an origin for these coronal lines in the inner part of the NLR or in the transition region between the BLR and the NLR, as suggested by previous authors (e.g. Rodriguez-Ardila et al. 2006). Ionization potentials for the parent species of each coronal line emitter are listed in Table 2. These generally support the formation of the observed stratified coronal emission region through photoionization by the central AGN, with higher ionization potential species located closer to the ionizing source. With photon energies of 127.2 eV being required to create Ca VIII, the smaller extent of the [Ca VIII] emission region when compared to that of the [Si VII], which has higher ionization potential, is unexpected. This fact can be attributed to depletion of calcium on to dust grains, which can alter the gas-phase calcium abundance by large factors (e.g. Groves et al. 2004a,b).

4.3 Molecular gas distribution

The H_2 intensity distribution is totally different from those of the other emission lines. It avoids the bicone (bottom-left panel of Fig. 6) and is more extended than other emission lines along the minor axis of the galaxy, which coincides approximately with the orientation of the bar. The H_2 emission covers a region ≈20–60 pc

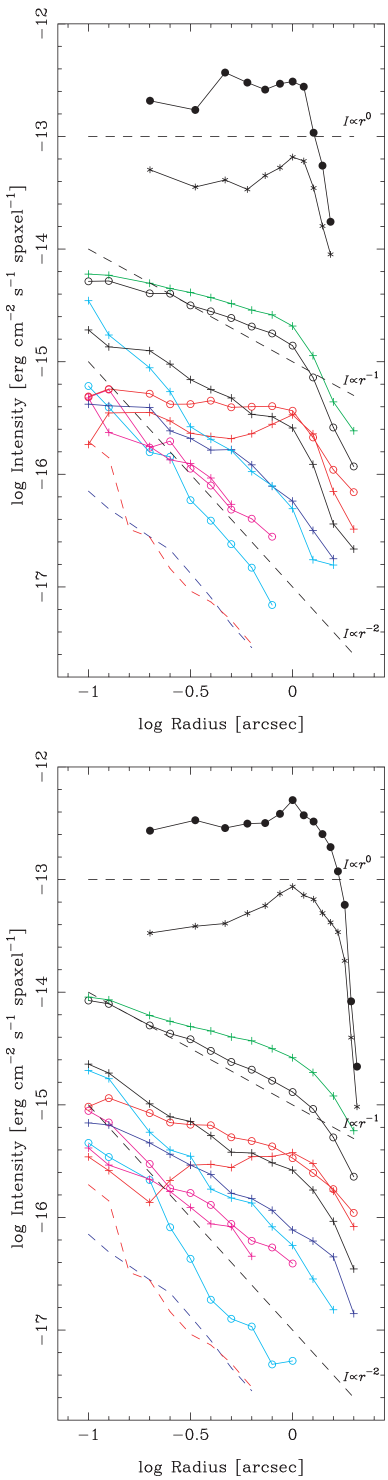

Figure 8. Radial emission-line profiles in cones of 40° opening angle at PA = 60° (top) and 240° (bottom) along the bicone axis; [Fe II] 1.257 μm (red crosses), [S II] 1.029/32/33 μm (red open circles), H I P*β* 1.282 μm (black crosses), [S III] 0.9533 μm (green crosses), He I 1.083 μm (black open circles), He II 1.013 μm (dark blue crosses), [O II] 0.3727 μm (black asterisks), [O III] 0.5007 μm (black filled circles), [Si VII] 2.483 μm (light blue crosses), [Ca VIII] 2.322 μm (light blue circles), [S VIII] 0.991 μm (magenta crosses), [S IX] 1.2523 μm (magenta open circles). Telluric star profiles in the *J* and *K* bands are shown in blue and red dashed lines, respectively. Black dashed lines illustrate the slopes corresponding to different radial dependencies for the intensity.

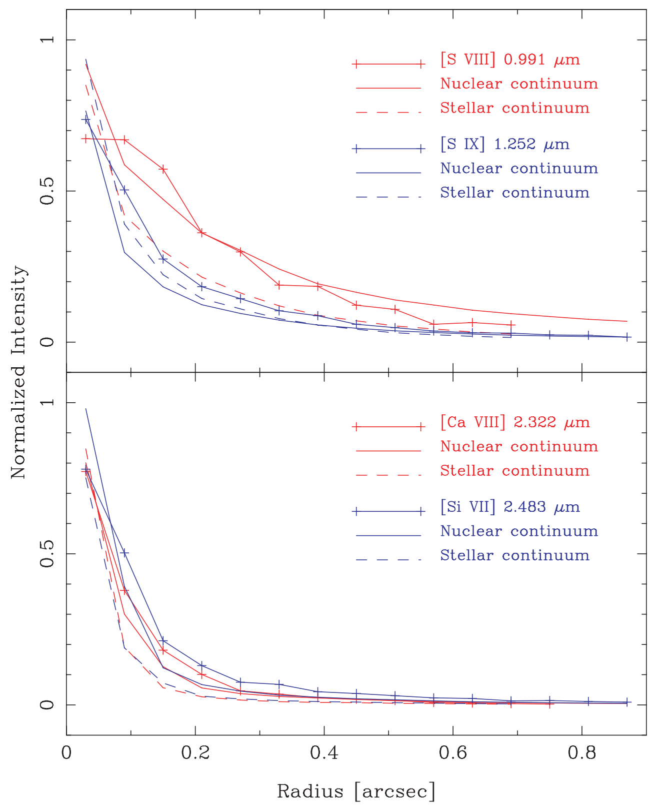

Figure 9. Comparison of the spatial profiles of a star in the *J* and *K* bands (dashed lines) with those of the galaxy nucleus in the *J* and *K* continuum and in the coronal lines [S IX], [S VIII], [Ca VIII] and [Si VII].

in radial extent from the nucleus. One possible explanation for this morphology is that the nuclear molecular gas is located predominantly in the plane of the galaxy, but is dissociated by the AGN radiation field within the bicone. It is known that the bicone intercepts part of the galaxy plane.[1] Perpendicular to the bicone, the H_2 must be shielded from the strongest dissociating radiation, probably by a dusty torus and/or by the walls of the bi-conical outflow (Kraemer et al. 2008).

A previous $H_2\,\lambda 2.1218$ μm image of the nuclear region of NGC 4151 was obtained by Fernandez et al. (1999) who found a similar intensity distribution to that of ours, in the form of a partial ring surrounding the nucleus, which led them to propose that the H_2 emission originated in the outer part of a molecular torus. They suggested that the H_2-emitting gas could be rotating in a plane perpendicular to the radio axis. We note, however, that the orientation of the partial ring shown in Fernandez et al. (1999) is rotated by 90° and is mirrored relative to our H_2 intensity distribution. Otherwise, the intensity distributions are consistent with each other considering the difference in spatial resolution [0.6 arcsec in Fernandez et al. (1999) and 0.11 arcsec here]. As our data cube gives intensity distributions for the ionized gas in agreement with that for the well-known bicone, and the H_2 intensity distribution is obtained from the same data cube, we conclude that the orientation of the H_2 ring is mistaken in Fernandez et al. (1999). Our observations also do not support the suggestion by these authors that the H_2 gas is rotating

[1] See Simões Lopes et al. (in preparation) and Das et al. (e.g. 2005) for a comprehensive discussion of the kinematics and geometry of the bicone and the galaxy.

Table 1. Emission-line fluxes within 0.3 × 0.3 arcsec^2 apertures (10^{-15} erg cm^{-2} s^{-1}).

λ (vac.)	ID	Nucleus	[Fe II] peak (0.9 arcsec SW)	H_2 peak (0.7 arcsec SE)	Pos. B (0.7 arcsec E)
0.95486	H I Pa ϵ (broad)†	87.91 ± 11.5	–	–	–
0.95332	[S III] $^1D_2$ $-^3P_2$ †*ger*	108.57 ± 17.7	42.91 ± 0.18	12.83 ± 0.09	38.63 ± 0.14
0.98268	[C I] $^1D_2$ $-^3P_1$	0.29 ± 0.16	0.22 ± 0.08	0.09 ± 0.05	0.40 ± 0.10
0.98530	[C I] $^1D_2$ $-^3P_2$	1.44 ± 0.39	0.84 ± 0.18	0.46 ± 0.09	0.59 ± 0.09
0.99154	[S VIII] $^2P^0_{1/2}$ $-^2P^0_{3/2}$	4.42 ± 0.29	0.83 ± 0.24	0.37 ± 0.10	0.62 ± 0.10
1.00521	H I Pa δ (narrow)	3.56 ± 0.34	1.52 ± 0.19	0.84 ± 0.15	1.61 ± 0.18
1.00521	H I Pa δ (broad)‡				
1.01264	He II $5-4$ (narrow)	4.34 ± 0.26	1.52 ± 0.20	0.57 ± 0.10	1.48 ± 0.12
1.01264	He II $5-4$ (broad)‡	114.56 ± 19.1	–	–	–
1.02895	[S II] $^2P^0_{3/2}$ $-^2D^0_{3/2}$	3.21 ± 0.34	0.89 ± 0.14	0.50 ± 0.10	1.12 ± 0.14
1.03233	[S II] $^2P^0_{3/2}$ $-^2D^0_{5/2}$	2.72 ± 0.32	1.02 ± 0.13	0.44 ± 0.10	1.16 ± 0.11
1.03392	[S II] $^2P^0_{1/2}$ $-^2D^0_{3/2}$	4.47 ± 0.44	1.31 ± 0.21	0.28 ± 0.10	1.06 ± 0.14
1.03733	[S II] $^2P^0_{1/2}$ $-^2D^0_{5/2}$	1.36 ± 0.26	0.31 ± 0.13	0.21 ± 0.07	0.50 ± 0.15
1.04006	[N I] $^2P^0_{3/2}$ $-^2D^0_{5/2}$	1.78 ± 0.37	0.20 ± 0.13	0.19 ± 0.12	0.26 ± 0.08
1.04100	[N I] $^2P^0_{1/2}$ $-^2D^0_{3/2}$	1.45 ± 0.31	0.07 ± 0.06	0.18 ± 0.10	0.44 ± 0.13
1.06706	He I ^3S $-^3P^0$	1.69 ± 0.43	0.13 ± 0.07	0.04 ± 0.04	0.32 ± 0.08
1.08332	He I $^3P^0$ $-^3S$ (narrow)	90.48 ± 3.21	22.95 ± 0.21	8.99 ± 0.11	30.36 ± 0.18
1.08332	He I $^3P^0$ $-^3S$ (broad)★	409.06 ± 13.29	–	–	–
1.09411	H I Pa γ (narrow)	7.01 ± 0.37	2.35 ± 0.19	0.95 ± 0.12	1.80 ± 0.11
1.09411	H I Pa γ (broad)★	–	–	–	–
1.12900	O I $^3D^0$ $-^3P$	0.53 ± 0.26	–	–	–
1.16296	He II $7-5$	2.65 ± 0.42	0.54 ± 0.17	0.31 ± 0.12	0.53 ± 0.15
1.18861	[P II] $^1D_2$ $-^3P_2$	2.49 ± 0.33	1.06 ± 0.17	0.28 ± 0.10	0.63 ± 0.10
1.25235	[S IX] $^3P_1$ $-^3P_2$	8.74 ± 0.38	0.52 ± 0.20	0.29 ± 0.10	0.39 ± 0.10
1.25702	[Fe II] a$^4D_{7/2}-a^6D_{9/2}$	6.41 ± 1.28	7.36 ± 0.18	1.44 ± 0.12	4.09 ± 0.26
1.27069	[Fe II] a$^4D_{1/2}-a^6D_{1/2}$	–	1.00 ± 0.32	–	0.19 ± 0.15
1.27912	[Fe II] a$^4D_{3/2}-a^6D_{3/2}$	0.11 ± 0.07	0.60 ± 0.16	0.15 ± 0.06	0.49 ± 0.20
1.28216	H I Pa β (narrow)	17.38 ± 0.38	4.15 ± 0.16	1.26 ± 0.08	2.61 ± 0.08
1.28216	H I Pa β (broad)	278.52 ± 10.86	–	–	3.35 ± 0.32
1.29462	[Fe II] a$^4D_{5/2}-a^6D_{5/2}$	–	0.78 ± 0.17	–	0.07 ± 0.05
1.29812	[Fe II] a$^4D_{3/2}-a^6D_{1/2}$	–	0.241 ± 0.02	–	0.03 ± 0.02
1.32814	[Fe II] a$^4D_{5/2}-a^6D_{3/2}$	1.65 ± 0.39	1.86 ± 0.17	0.38 ± 0.11	0.50 ± 0.12
1.53389	[Fe II] a$^4D_{5/2}-a^4F_{9/2}$	2.21±1.71	0.89 ± 0.22	–	0.63 ± 0.31
1.59991	[Fe II] a$^4D_{3/2}-a^4F_{7/2}$	–	0.48 ± 0.20	–	0.11 ± 0.09
1.64117	H I Br 12 (total)	29.34 ± 5.3	–	–	–
1.64400	[Fe II] a$^4D_{7/2}-a^4F_{9/2}$	6.2 ± 1.2	6.11 ± 0.19	1.29 ± 0.12	3.27 ± 0.17
1.66423	[Fe II] a$^4D_{1/2}-a^4F_{5/2}$	–	0.25 ± 0.17	0.17 ± 0.03	0.21 ± 0.05
1.67734	[Fe II] a$^4D_{5/2}-a^4F_{7/2}$	–	0.56 ± 0.19	–	0.04 ± 0.03
1.68111	H I Br 11 (total)	32.29 ± 8.2	–	–	–
1.73669	H I Br 10 (total)	0.86 ±15.2	–	–	0.43 ± 0.17
1.74801	H_2 $1-0\,S(7)$	–	0.13 ± 0.12	0.26 ± 0.06	0.08 ± 0.09
1.74890	[Fe II] a$^4P_{3/2}-a^4D_{7/2}$	–	0.12 ± 0.20	–	0.03 ± 0.02
2.03376	H_2 $1-0\,S(2)$	–	0.19 ± 0.16	0.48 ± 0.04	0.27 ± 0.06
2.05869	He I $^1P^0$ $-^1S$	–	0.36 ± 0.15	0.17 ± 0.06	0.43 ± 0.07
2.07498	H_2 $2-1\,S(3)$	–	–	0.13 ± 0.02	0.07 ± 0.02
2.12183	H_2 $1-0\,S(1)$	–	0.42 ± 0.15	1.21 ± 0.03	0.55 ± 0.04
2.15420	H_2 $2-1\,S(2)$	–	–	0.09 ± 0.05	0.04 ± 0.04
2.16612	H I Br γ (narrow)	5.22 ± 0.40	0.85 ± 0.13	0.34 ± 0.04	0.80 ± 0.05
2.16612	H I Br γ (broad)	39.34 ± 3.25	–	–	–
2.20133	H_2 $3-2\,S(3)$	–	–	0.01 ± 0.01	0.02 ± 0.02
2.22344	H_2 $1-0\,S(0)$	–	0.27 ± 0.13	0.28 ± 0.02	0.13 ± 0.03
2.24776	H_2 $2-1\,S(1)$	–	–	0.14 ± 0.02	0.08 ± 0.04
2.32204	[Ca VIII] $^2P^0_{3/2}$ $-^2P^0_{1/2}$	3.81 ± 0.42	0.15 ± 0.08	0.13 ± 0.01	0.34 ± 0.03
2.40847	H_2 $1-0\,Q(1)$	–	0.27 ± 0.07	1.15 ± 0.01	0.51 ± 0.01
2.41367	H_2 $1-0\,Q(2)$	–	0.08 ± 0.06	0.33 ± 0.01	0.12 ± 0.01
2.42180	H_2 $1-0\,Q(3)$	–	0.63 ± 0.08	0.49 ± 0.01	0.17 ± 0.01
2.43697	H_2 $1-0\,Q(4)$	–	–	0.33 ± 0.01	0.21 ± 0.01
2.45485	H_2 $1-0\,Q(5)$	–	–	0.74 ± 0.01	0.25 ± 0.01
2.47555	H_2 $1-0\,Q(6)$	–	–	0.21 ± 0.01	0.13 ± 0.01
2.48334	[Si VII] $^3P_1$ $-^3P_2$	14.29 ± 0.39	1.21 ± 0.07	1.17 ± 0.02	2.68 ± 0.01
2.50007	H_2 $1-0\,Q(7)$	–	–	0.49 ± 0.01	0.20 ± 0.01

†Narrow component of P ϵ blended with [S III]λ 0.9533.
‡Broad component of Pa δ blended with broad component of He I λ 1.01264.
★Broad component of Pa γ blended with He I λ1.08332.

Table 2. Ionization potentials.

Line	IP (eV)
[Fe II]	7.9
[S II]	10.4
[P II]	10.5
[S III]	23.3
[Ca VIII]	127.2
[Si VII]	205.3
[S VIII]	280.9
[S IX]	328.8

in a plane perpendicular to the radio jet. In Simões Lopes et al. (in preparation), we present the H_2 kinematics which show very little rotation consistent with a gas distribution in the galaxy plane along the minor axis. Nevertheless, our observations are consistent with the interpretation that the H_2-emitting gas may be tracing the gas reservoir which feeds the super massive black hole. Results supporting this idea are the inflows measured by Mundell & Shone (1999) in radio observations of H I along the large-scale bar (at PA = 130°). These inflows direct gas towards the inner part of the bar in the nuclear region, and their orientations are approximately perpendicular to the arc-shaped structures delineated by the H_2 light distribution (see Fig. 6). Thus, one possibility is that the radio observations are tracing H I inflows towards the nuclear region leading to the build up of the molecular gas reservoir which we observe in the H_2 intensity distribution.

4.4 Extinction

Previous studies report low reddening towards the NLR of NGC 4151. Crenshaw & Kraemer (2005) claim only low Galactic extinction of $E(B-V) = 0.02 \pm 0.04$ mag in Space Telescope Imaging Spectrograph (STIS) spectra centred on the 'nuclear emission-line knot'. Kraemer et al. (2000) report that at other locations in the NLR the optical reddening of the emission lines ranges from $E(B-V) \approx 0.0$ to 0.4.

Other studies (e.g. Alexander et al. 1999) report reddening estimates which range from almost negligible $E(B-V) = 0.04$–0.05) (e.g. Penston et al. 1981; Kriss et al. 1995) to the considerable $E(B-V) = 0.13$ (Malkan 1983). From a variety of methods (and data), including near-IR emission lines, Ward et al. (1987) get $E(B-V) \sim 0.23$ mag, while Rieke & Lebofsky (1981) obtain $0.5 < A_V < 0.8$.

Mundell et al. (1995) measure H I absorption to the radio component C_4 of 3.9×10^{21} cm^{-2}. From Bohlin, Savage & Drake (1978) $\langle N(\mathrm{H\,I}+H_2)/E(B-V)\rangle = 5.8 \times 10^{21}$ cm^{-2} mag^{-1}, so this H I column corresponds to $E(B-V) = 0.7$ ($A_V \sim 2.1$ mag) to the nuclear radio source, if there is no intervening H_2.

We can use the line-ratio map [Fe II] $\lambda 1.2570/\lambda 1.6440$ to estimate the reddening to the NLR of NGC 4151. These lines arise from the same upper level so the intrinsic value of the line ratio should be 1.36, according to the transition probabilities of Nussbaumer & Storey (1988) and as confirmed from observations by Bautista & Pradhan (1998). Smaller line ratios indicate the presence of reddening and can be used to estimate its value through the relation:

$$E(B-V) = 8.14 \times \log\left[\frac{1.36}{(F_{1.2570})/(F_{1.6440})}\right] \quad (1)$$

obtained using the reddening law of Cardelli, Clayton & Mathis (1989).

Typical values of the reddening uncertainty can be obtained from the data in Table 1. The measured flux ratios are 1.21 ± 0.06 and 1.25 ± 0.12 for the SW [Fe II] peak and Position B, respectively. These ratios equate to $E(B-V) = 0.41 \pm 0.14$ and 0.30 ± 0.28, from which we estimate random uncertainties in $E(B-V)$ derived by this method to be $\approx \pm 0.2$ mag along the radio axis. For the nucleus and other regions where the [Fe II] emission is weaker, the uncertainties are twice as large.

In order to further investigate the reddening variation across the NLR, we have extracted smoothed 1D profiles from the [Fe II]$\lambda 1.644$ and 1.257 μm intensity maps along a pseudo-slit of width 0.3 arcsec, oriented along the bicone. The fluxes were obtained at each 0.1 arcsec along the pseudo-slit as the average of the fluxes of the pixels included within the 0.3 arcsec width of the slit. The 1D profiles were then smoothed further by replacing the flux at each position by the average of its flux and those of the two adjacent positions along the slit. We have then constructed the ratio between the two 1D profiles along the bicone and obtained the $E(B-V)$ from the expression above. The result is shown in the upper-right panel of Fig. 10, showing a maximum $E(B-V) = 1.4$ at the nucleus, which decreases abruptly to values in the range $0.3 < E(B-V) < 0.6$ beyond 0.2 arcsec from the nucleus, with an average value of $E(B-V) \approx 0.45$.

In order to check the above result, we have next used the Pa β/Br γ ratio to estimate the reddening along the same pseudo-slit, using the relation:

$$E(B-V) = 4.74 \times \log\left(\frac{5.88}{F_{P\beta}/F_{Br\gamma}}\right) \quad (2)$$

where we have again used the reddening law of Cardelli et al. (1989) and adopted the intrinsic $F_{P\beta}/F_{Br\gamma}$ ratio of 5.88 corresponding to case B recombination (Osterbrock 1989). Due to the somewhat longer wavelength baseline, the uncertainties in the resulting $E(B-V)$, of ± 0.15, are smaller than that obtained using the [Fe II] ratio. The results are shown in the bottom-right panel of Fig. 10. Within the uncertainties, the $E(B-V)$ values and spatial variation are similar to those obtained using the [Fe II] ratio: the highest values are observed at the nucleus, falling abruptly outwards to an average value around $E(B-V) \approx 0.5$.

We note that the nuclear $E(B-V)$ values are in agreement with the one obtained by Mundell et al. (1995) for the nuclear source, while $E(B-V) \approx 0.5$ is consistent with the highest $E(B-V)$ values obtained by Kraemer et al. (2000), considering also the fact that the optical depth reached in the near-IR is larger than those obtained by optical observations. Finally, we pointed out at the end of Section 3.2 that there may be a relation between the [Fe II]$\lambda 1.257/1.644$ map and the [O III] intensity distribution. In terms of reddening distribution, this relation would imply that the regions with largest reddening would coincide with the gaps in the intensity distribution, suggesting that the appearance of the [O III] intensity distribution could be, at least in part, due to reddening. As $E(B-V) \approx 0.5$ has been obtained from smoothed profiles, this value is consistent with higher extinction in narrow structures not resolved by these smoothed profiles. For example, if the average $E(B-V) \approx 0.5$ is due to the smoothing of narrow strands having $E(B-V) = 1$, with $E(B-V) = 0$ between the strands, the [O III] flux will be reduced by a factor of ≈25 where $E(B-V) = 1$, which could result in the stranded appearance observed in the [O III] intensity distribution. Data with better spatial resolution and higher signal-to-noise ratio would be necessary in order to test this possibility.

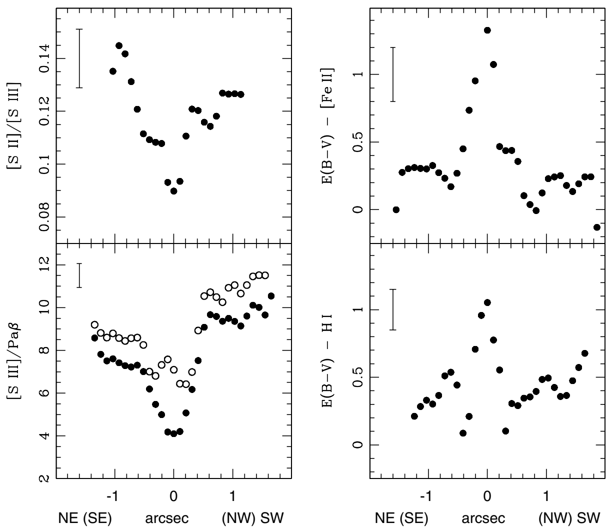

Figure 10. Left-hand panel: spatial line-ratio profiles along the bicone axis (PA = 60°) obtained from smoothed 1D profiles extracted within a pseudo-slit of width 0.3 arcsec. Filled circles show values not corrected for reddening, while the open circles show values corrected for reddening with $E(B-V)$ obtained from the average of the two $E(B-V)$ values from the right-hand panels for each location. Right-hand panel: $E(B-V)$ values obtained from the line-ratio profiles of [Fe II]λ1.257/1.644 (top) and Pa β/Br γ (bottom).

4.5 Gas excitation

The line-ratio [S III]/Paβ (top-right panel of Fig. 7) can be used as a tracer of the excitation of the NLR gas. We have obtained typical values for this line ratio in active and starburst galaxies from the works of Storchi-Bergmann, Kinney & Challis (1995) and Riffel et al. (2006a). In the case of Storchi-Bergmann et al. (1995), we have used their observed [S III]/Hα ratio values (not corrected for reddening) to estimate the [S III]/Paβ ratios [assuming a typical reddening of $E(B-V) = 0.5$], while in the case of Riffel et al. (2006a) we have used their measured values for [S III] and Paβ fluxes, also not corrected for reddening. In order to avoid the contribution of the broad components to the emission lines, we have collected only the values for Seyfert 2 galaxies as typical of the NLR, as well as those for starburst galaxies, to use as a comparison. The range of line ratios obtained for a total sample of 14 Seyfert 2 galaxies is $6 \leq$ [S III]/Pa$\beta \leq 14$, with most values clustering around [S III]/Pa$\beta \approx 8.5$, while for a sample of 10 starburst galaxies the observed range is $1 \leq$ [S III]/Pa$\beta \leq 3.5$. These values can be compared to those in Fig. 7. In order to make such a comparison easier, we present, in the bottom panel of Fig. 10, line-ratio profiles along the bicone axis obtained from smoothed 1D profiles extracted along a pseudo-slit of width 0.3 arcsec, as described in the previous section.

In the 1D profiles of Fig. 10, the observed [S III]/Paβ line ratios (filled circles) beyond 0.5 arcsec from the nucleus are in the range 7–10, thus similar to the values for NLR of Seyfert 2 galaxies, with the values to the NE being 20–30 per cent smaller than those to the SW. Within 0.5 arcsec from the nucleus, the line ratio decreases down to half the values beyond this region. This decrease is partially due to reddening, as can be observed in the reddening-corrected line-ratio profile shown as open circles in the bottom-left panel of Fig. 10. The corrected values were obtained by again using the reddening law of Cardelli et al. (1989) and the $E(B-V)$ for each location as the average of the two values shown in the right-hand panels of Fig. 10. The values of the line ratio within 0.5 arcsec from the nucleus increase from 4–6 to 7–8, now within the typical range observed for AGN. Nevertheless, the correction for reddening does not completely eliminate the decrease observed at the nucleus, and another effect may be present, possibly a residual contribution of the broad component of Hβ. In principle, the 20–30 per cent smaller [S III]/Paβ values to the NE relative to the SW could also be due to an excess reddening of $E(B-V) \approx 0.5$. Nevertheless, the $E(B-V)$ profiles in the right-hand panels of Fig. 10 do not show a systematic difference in reddening between the SW and NE of this order, and we thus attribute the lower ratios to NE to lower excitation.

The [S II]/[S III] ratio (top-left panel of Fig. 7) can also be used as a tracer of the excitation, although this ratio is noisier than the [S III]/Paβ ratio due to the fact that the [S II] flux map is a collection of the fluxes in four faint emission lines. We have also constructed a 1D line-ratio spatial profile for [S II]/[S III], which is shown in the top-left panel of Fig. 10. Beyond 0.5 arcsec from the nucleus, this ratio is higher to the NE, which indicates lower excitation relative to the SW side of the bicone, in agreement with the behaviour of the [S III]/Paβ ratio. Within 0.5 arcsec from the nucleus, the [S II]/[S III] ratio decreases, which cannot be attributed to reddening, as an excess reddening should increase the value of this line ratio and not decrease. Although this decrease could be due to a higher excitation in this region, this is not consistent with the behaviour of the [S III]/Paβ line ratio. Our favoured explanation is as follows. In the next section, we use the observed [Fe II] line ratios to derive the electronic density along the NLR. Within ≈0.5 arcsec from the nucleus, the average density (see Fig. 12) is higher than the critical density of [S II] (2.5×10^4 cm^{-3}), resulting in a decrease in the intensity of the [S II] lines close to the nucleus.

How can one understand the lower excitation to the NE as compared to the SW side of the cone? According to previous models (e.g. Hutchings et al. 1998; Crenshaw et al. 2000; Das et al. 2005), the gas in the NLR is outflowing along a hollow cone, with the SW side tilted towards us. Our line of sight is almost along, but outside, the near edge of the SW cone. As the cone seems to have a geometrical cut-off at ≈100 pc from the nucleus, we are looking at the inner wall of the cone to the SW, while to the NE we are looking at the outer wall of the cone, which is at least partly behind the plane of the galaxy. We see higher excitation when we look at the inner wall of the cone and somewhat lower excitation when we look at the outer wall of the cone. As we do not see any reddening difference between the two sides of the cone, the only explanation seems to be that the ionizing radiation is attenuated more to the NE than to the SW.

Recently, Kraemer et al. (2008) have mapped the ionization in the NLR of NGC 4151 using the line-ratio map [O III]]/[O II] obtained from the ratio of narrow-band *HST* images. They compare the observed emission-line ratios along the NLR with photoionization models and point out that, while the highest line ratios are observed along the bicone, there is also emission from regions outside the cone, with smaller line ratios, indicating lower excitation. They attribute this lower excitation to a weaker ionizing flux reaching these regions due to the presence of a 'low-ionization absorber' which filters the radiation. This absorber seems to be ionized gas, leading Kraemer et al. (2008) to propose that the low-ionization absorbers are dense knots of gas swept up by an accretion disc wind.

Our excitation maps do not seem to show a decrease of the excitation perpendicular to the bicone as observed by Kraemer et al. (2008). Instead, we find lower excitation to the NE than to the SW, as discussed above. Maybe the difference between our results and those of Kraemer et al. (2008) can be attributed to the different optical depths probed by optical and near-IR observations. The difference in excitation between the NE and SW sides of the bicone could then be due to the presence of more absorbers between the nuclear ionizing source and the emitting gas we see to the NE than to the SW.

4.6 Physical conditions of the [Fe II] emitting region

There are many [Fe II] emission lines in our near-IR spectra of the NLR of NGC 4151, especially to the SW, where the [Fe II] emission is strongest. The near-infrared [Fe II] emission lines are due to forbidden transitions between low energy levels, and their intensities are thus principally dependent on the electron density. We were able to measure four [Fe II] line ratios in the region of strongest [Fe II] emission (at ≈0.9 arcsec SW of the nucleus), from the fluxes listed in Table 1, which can be used as density indicators. We have performed a 16-level atom calculation for [Fe II] and have obtained line intensities in order to compare with the observed ones in NGC 4151 and derive the electron density. Fig. 11 shows the model results for four emission-line ratios as a function of the electron density for different values of the electronic temperature, along with the measured ratios and uncertainties. The line ratios indicate a density in the region of the strongest [Fe II] emission of ≈4000 cm^{-3}.

Most of the [Fe II] emission-line ratios that are density indicators could be measured only at the location of maximum [Fe II] emission. The exception is [Fe II]1.533/1.644, which could be measured at several other locations allowing the construction of an electron density map, shown in Fig. 12. The uncertainty in the line flux of the 1.533 μm line is quite large at the nucleus (see Table 1), but decreases outwards. It can be concluded from Fig. 12 that the electronic density in the [Fe II] region decreases from the highest values at the nucleus ($\geq 10^5$ cm^{-3}) to $\approx 10^4$ cm^{-3} within the inner ≈0.5 arcsec from the nucleus. Outside this radius, the density reaches the value of ≈4000 cm^{-3} obtained above.

Deriving the electron temperature in the [Fe II] emitting region is more difficult, as most observable emission lines arise from a limited range of upper level energies. Following Mouri, Kawara & Taniguchi (2000) and McGregor et al. (in preparation), we looked for emission lines corresponding to transitions from the a^4P term. There is a transition between the terms $^4P_{4/3}$ and $a^4D_{7/2}$ corresponding to an emission line at 1.7489 μm in the *H* band. Although we have apparently detected this line, its uncertainty is too large to put a useful constraint on the electron temperature. Another possibility suggested by Thompson (1995) is to use the [Fe II] 0.8619 μm line strength, corresponding to the transition $a^4P_{5/2}$–$a^4F_{9/2}$ as an indicator of the electron temperature. Unfortunately, our observed spectral range does not cover this emission line, and we had to look for previous observations available in the literature in which this line was measured. Osterbrock et al. (1990) have identified the [Fe II] 0.8619 μm emission line in their spectrum of NGC 4151, reporting a flux ratio [Fe II] 0.8619/[S III] 0.9533 = 0.042. We have used this ratio and our measurement of the [S III] 0.9533 line flux at 0.9 arcsec SW from the nucleus in order to estimate the flux of the [Fe II] 0.8619 emission line at this location, under the assumption

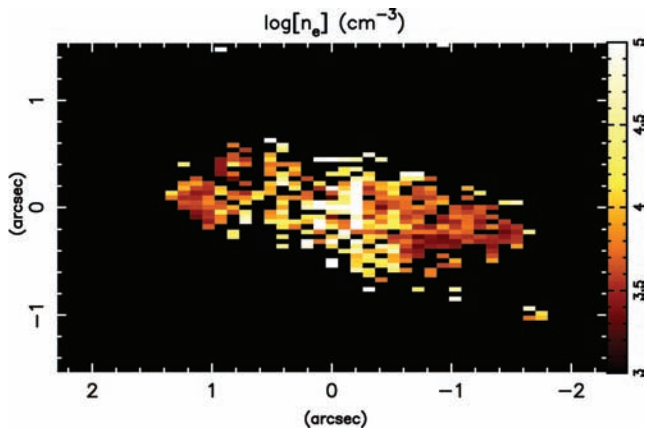

Figure 12. Distribution of electron density N_e obtained from the [Fe II] 1.533/1.644 emission-line ratio, for an electron temperature in the range $5000 < T_e < 20\,000$ K.

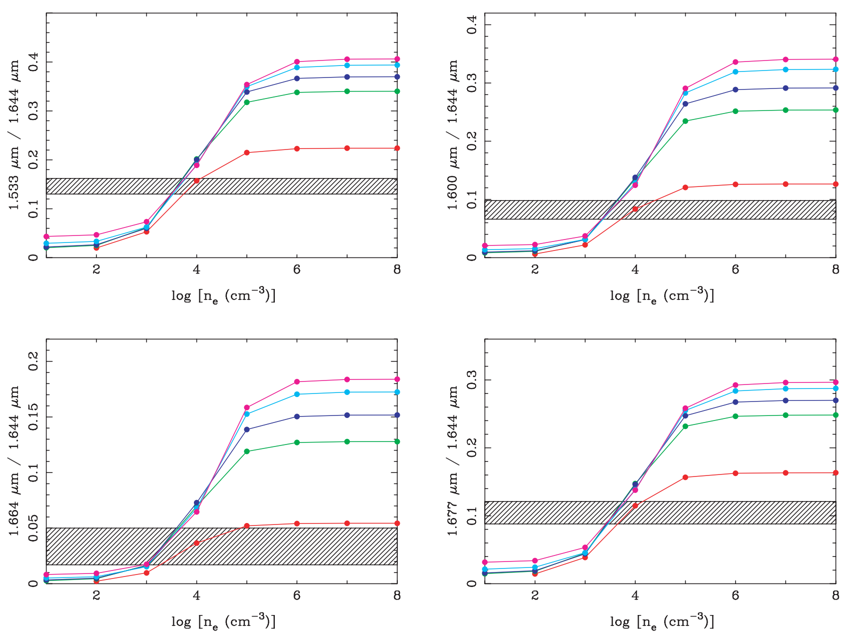

Figure 11. Model [Fe II] emission-line ratios versus electron density. Each sequence of models corresponds to a different temperature – from bottom to top – 1, 3, 5, 10 and 20 × 10^3 K. The shaded regions correspond to the measured line ratio and their uncertainties within a region of aperture 0.3 × 0.3 $arcsec^2$ centred in the [Fe II] emission peak at 0.9 arcsec SW from the nucleus.

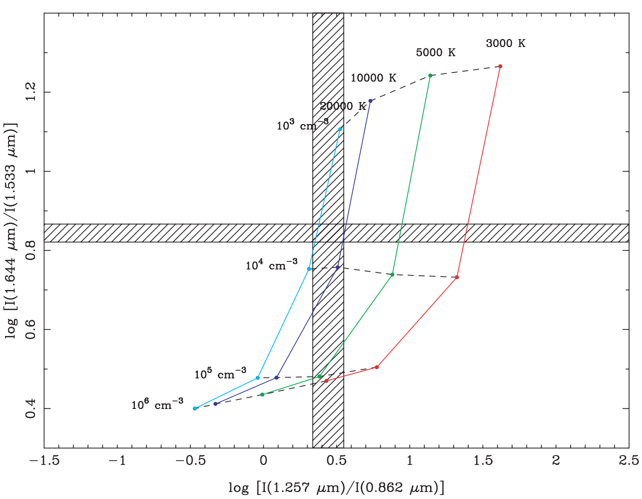

Figure 13. Model [Fe II] line ratio 1.644/1.533 μm (which depends mostly on the gas density) versus the line ratio 1.257/0.862 μm (which depends mostly on the temperature) as a function of density and temperature. The shaded region corresponds to the measured line ratios and their uncertainties within a region of aperture 0.3 × 0.3 arcsec^2 centred in the [Fe II] emission peak at 0.9 arcsec SW from the nucleus.

that the [Fe II] 0.8619/[S III] 0.9533 ratio is the same as that obtained by Osterbrock et al. (1990), in spite of their much larger aperture. Using the fluxes from Table 1, we obtain [Fe II] 0.8619 = 2.09 $\times$ 10^{-15} erg cm^{-2} s^{-1}, and thus a ratio [Fe II] 1.2570/0.8619 = 3.6. If we consider a reddening value $E(B-V) \approx 0.5$, the corrected log([Fe II] 1.2570/0.8619) = 0.46 ± 0.11 and the resulting temperature will be 15 000 ± 5000 K, as illustrated in Fig. 13 (considering the uncertainties in the line ratio combined with those in the reddening correction).

The origin of [Fe II] emission in galaxies has been the subject of many studies, since the finding by Forbes & Ward (1993) and Blietz et al. (1994) of a correlation between the [Fe II] and radio emission. This suggests that shock excitation by radio jets is a likely mechanism for the production of the [Fe II] emission (Dopita & Sutherland 1995, 1996). However, subsequent works have argued that the dominant excitation mechanism is photoionization, with shock excitation accounting for only ≈20 per cent of the [Fe II] excitation in AGN (Simpson et al. 1996).

An important tracer of the origin of the [Fe II] emission is the line-ratio [Fe II]/Paβ, whose value ranges from <0.6 for starbursts to >2 for supernova remnants, for which shocks are the dominant mechanism (Rodriguez-Ardila et al. 2004). Active galaxies have values for this ratio between 0.6 and 2, suggesting that for ratios close to 0.6 photoionization is the dominant mechanism, while for ratios close to 2, shock excitation dominates (Storchi-Bergmann et al. 1999; Rodriguez-Ardila et al. 2004). [Fe II]/Paβ ratios ≥2 have been found by Riffel et al. (2006b) in a near-IR IFU study the NLR of the Seyfert 2 galaxy ESO 428–G14 in regions showing a close association with emission knots of a radio image, supporting an origin for the [Fe II] emission in shocks produced by the radio jet.

In NGC 4151, [Fe II]/Paβ ≤ 1 within the inner 0.6 arcsec, increasing to values of ≈2 outwards (see Fig. 7), suggesting that photoionization dominates in the inner region while shocks dominate in the outer region. Indeed, the inspection of the [Fe II]/Pa β ratio map in Fig. 7 shows a relation with the radio structure: to the SW, the increase in the [Fe II]/Paβ ratio does coincide with a flaring in the radio contours, which may have been produced by a shock between the jet and ambient gas, while to the NE, a similar increase is observed at the location of a radio knot.

Another powerful indicator of the origin of the [Fe II] emission is the [Fe II] 1.2570/[P II] line ratio, as pointed out by Oliva et al. (2001). This line ratio is seldom used because the [P II] emission line is usually too faint. The quality of our data has allowed the measurement of extended emission in this line. Besides having similar wavelengths, the [Fe II] 1.2570 and [P II] lines have similar excitation temperatures, and their parent ions have similar ionization potentials and radiative recombination coefficients. Oliva et al. (2001) have shown that, for a solar abundance, the above ratio is >20, as observed in supernova remnants. But, in many astronomical objects this ratio is much smaller, because Fe is locked into grains. For example, in Orion, the above ratio is ≈2. In order to destroy the dust grains and release the Fe, fast shocks are necessary. Larger ratios than 2 indicate that shocks have passed through the gas destroying the dust grains, releasing the Fe and thus enhancing its observed abundance. Oliva et al. (2001) have reported the first observation of this line ratio in an extragalactic source, and here we report the first 2D map of this ratio in an extragalactic source. In NGC 4151, [Fe II]/[P II] varies from 2 to 6, with the highest values observed in patches which do seem to be spatially correlated with the radio structure, as shown in Fig. 7: the highest ratios are observed at the location of a radio knot to the NE and at ≈0.8 arcsec SW from the nucleus, where the flaring of the radio contours is observed. These locations also coincide with those where the ratio [Fe II]/Paβ shows the highest values, supporting an increased contribution of shocks to the excitation of [Fe II] at these locations. Nevertheless, the [Fe II]/[P II] line ratio is never as high as ≈20, which suggests that the excitation mechanism is not only shocks, but also includes photoionization.

4.7 Physical conditions of the H_2 emitting region

As discussed by Riffel et al. (2006b), the H_2 emission lines can be excited by two processes: (1) fluorescence by soft-UV photons (Black & van Dishoeck 1987) – present both in star-forming regions and in around active nuclei, or (2) thermal processes, produced either by X-ray (Maloney, Hollenbach & Tielens 1996) or by shock heating (Hollenbach & McKee 1989).

An emission-line ratio commonly used to investigate the origin of the H_2 excitation is H_2 2.1218/Br γ. In starburst galaxies, where the main heating agent is UV radiation, H_2/Brγ < 0.6 (Rodriguez-Ardila et al. 2004), while for Seyferts this ratio is larger because of additional thermal excitation by shocks or X-rays from the AGN. As observed in Fig. 7, this line ratio is <1 around the nucleus and along the axis of the bicone, but increases to values >2 and up to 4 along the minor axis of the galaxy (and approximately perpendicular to the bicone axis). By comparing Fig. 7 with Fig. 6 which shows that the H_2 intensity distribution avoids the region along the bicone axes, we propose that the low H_2/Brγ ratio in these regions is due to the destruction of the H_2 molecule by the strong radiation and particle fluxes, while the high values at the perpendicular direction could be due to fluorescence or to excitation by nuclear X-rays escaping in that direction or by shocks. In the case of NGC 4151, shocks in the region where H_2 emission is observed, perpendicular to the radio jet, can be produced in gas flowing into the nuclear region or associated with star formation in the disc. It could be even possible that star formation is occurring in in-flowing gas.

The H_2 λ2.2477/λ2.1218 line ratio can be used to distinguish between thermal (∼0.1–0.2) and fluorescent (∼0.55)

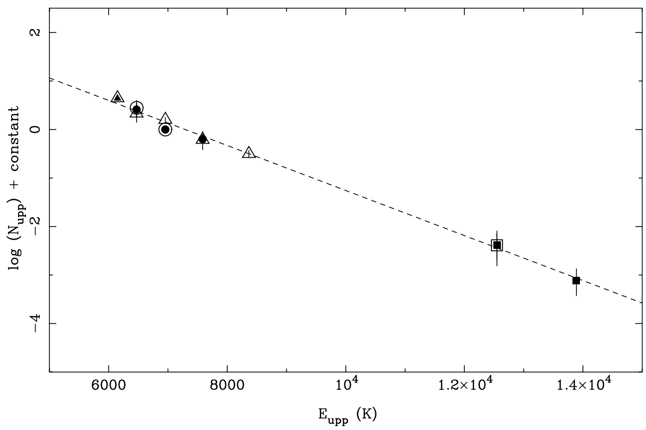

Figure 14. Relation between $N_{\rm upp} = (F_i\ \lambda_i)/(A_i g_i)$ and $E_{\rm upp} = T_i$ for the H_2 emission lines for thermal excitation at temperature $T_{\rm exc}$ =2155 K. Transitions plotted are from (left- to right-hand side) 1–0 Q(1), 1–0 S(0), 1–0 Q(2), 1–0 S(1), 1–0 Q(3), 1–0 S(2), 1–0 Q(4), 1–0 Q(5), 2–1 S(1) and 2–1 S(3).

excitation (Mouri 1994; Reunanen, Kotilainen & Prieto 2002; Rodriguez-Ardila et al. 2004). The first line could be measured in a few locations along the NLR. The resulting line ratio does not vary much along the NLR, and the average value is 0.13 ± 0.02, supporting a thermal excitation for the H_2.

We can investigate further the excitation mechanism of H_2 by using all its emission-line fluxes in the *K* band to calculate its excitation temperature $T_{\rm exc}$ and the ratio of the *ortho* to *para* emission lines. As the H_2 emission-line ratios seem not to show spatial variation, in order to improve the signal-to-noise ratio, we have measured the H_2 fluxes within a 0.5 arcsec diameter aperture centred on the SE peak of the H_2 intensity distribution. Following Wilman, Edge & Johnstone (2005), we have investigated the relation:

$$\log\left(\frac{F_i\lambda_i}{A_i g_i}\right) = \text{constant} - \frac{T_i}{T_{\rm exc}}, \qquad (3)$$

where F_i is the flux of the *i*th H_2 line, λ_i is its wavelength, A_i is the spontaneous emission coefficient, g_i is the statistical weight of the upper level of the transition and T_i is the energy of the level expressed as a temperature. This relation is valid for thermal excitation, under the assumption of an *ortho*:*para* abundance ratio of 3:1. $T_{\rm exc}$ (the reciprocal of the slope) will be the kinetic temperature if the H_2 is in thermal equilibrium.

The above relation is plotted in Fig. 14 where we have included the fluxes of most H_2 emission lines, excluding only the weakest ones [1–0 Q(6), 1–0 Q(7) and 2–1 S(1)]. The result is a tight straight line with $T_{\rm exc} = 2155$ K. The fact that all emission lines are on the relation confirms that the H_2 is in thermal equilibrium at $T_{\rm exc}$, and that the rotational and vibrational temperatures are the same, ruling out a significant contribution from fluorescence. The fact that the *ortho* lines [1–0 S(1), 2–1 S(1), 1–0 Q(1), etc.] give the same result as the *para* lines [1–0 S(0), Q(2), Q(4), etc.] confirms that the *ortho* to *para* ratio is ∼3 as assumed. This is also what is expected for thermal equilibrium.

We have thus concluded that the H_2 emission-line ratios are consistent with thermal excitation, which excludes UV fluorescence from the nucleus as a mechanism to excite the H_2 emission. But there are two other possibilities: heating by nuclear X-rays or by shocks in the gas flowing to the nucleus.

In order to test if X-rays from the AGN can account for the observed H_2 line fluxes, we have used the models of Maloney et al. (1996) to estimate the H_2 flux emitted by a gas cloud illuminated by a source of hard X-rays with luminosity $L_{\rm X}$. The calculations are performed as described in Zuther et al. (2007) and Riffel et al. (2008). Using an X-ray flux of 4.51×10^{-11} erg cm^{-2} s^{-1} and an absorption column density of 7.5×10^{22} cm^2 for the nuclear source (Cappi et al. 2006), we obtain an X-ray flux at a typical distance from the nucleus of 33 pc (0.5 arcsec from the nucleus, where H_2 emission is observed) of 7.3 erg cm^{-2} s^{-1} and an effective ionization parameter of $\xi_{\rm eff} = 0.015$. Using fig. 6(a) from Maloney et al. (1996), we can then estimate the resulting H_2 flux at the Earth for an aperture corresponding to our pixel of 0.1 × 0.04 arcsec – which gives a solid angle of 9.6×10^{-14} sr – as 7×10^{-15} erg cm^{-2} s^{-1}. Inspection of Fig. 6 shows that the highest values observed are $\approx 10^{-16}$ erg cm^{-2} s^{-1}, and we conclude that excitation by X-rays emitted by the AGN can account for most of the observed H_2 flux if a similar X-ray flux to that escaping in our direction also reaches the region of H_2 emission.

Prestwich, Wright & Joseph (1992) analysed near-infrared spectra of NGC 4151 obtained with >5.4 arcsec diameter apertures over a 10 year period from 1979 to 1989, and found that the H_2 line emission was stable over this interval while the (broad) H I Brγ emission varied significantly. This could argue against nuclear X-ray heating. However, the light crossing time of the H_2-emitting region with its ∼1 arcsec radial extent (Fig. 6) is ∼ 200 years, so nuclear variations on decade time-scales will be spatially diluted in large aperture measurements. Observations of individual H_2 clumps at higher angular resolution than possible with NIFS would be required to provide tighter constraints since the light crossing time of a 0.1 arcsec diameter clumps is still ∼20 years.

What then is powering the H_2 emission? Our observations are consistent with two mechanisms: X-rays from the active nucleus and/or shocks in the inner galactic disc, possibly produced by the accretion flow along the large-scale bar (Mundell et al. 1995), which may be the origin of the H_2 gas accumulated in the inner region.

4.8 Mass of ionized and molecular gas

The mass of ionized hydrogen can be estimated as $M_{\rm H\,II} = m_{\rm p}\, N_{\rm e}\, V_{\rm H\,II}$, where $N_{\rm e}$ is the electron density and $V_{\rm H\,II}$ is the volume of the emitting region.

The product $N_{\rm e}^2\, V_{\rm H\,II}$ can be obtained from the expression for the Brγ flux obtained using the H I emission coefficients listed in Osterbrock (1989):

$$F_{\rm Br\gamma} = 2.7 \times 10^{-28}\, \frac{N_{\rm e}^2 V_{\rm H\,II}}{D^2}\ \text{erg cm}^{-2}\,\text{s}^{-1}, \qquad (4)$$

where D is the distance to the galaxy in cm; units of density are cm^{-3} and we have assumed an electron temperature of 10^4 K and density in the range $10^2 < N_{\rm e} < 10^4$ cm^{-3}. The resulting gas mass in solar masses is

$$M_{\rm H\,II} = 3 \times 10^{19} \left(\frac{F_{\rm Br\gamma}}{\text{erg cm}^{-2}\,\text{s}^{-1}}\right)\left(\frac{D}{\text{Mpc}}\right)^2 \left(\frac{N_{\rm e}}{\text{cm}^{-3}}\right)^{-1}. \qquad (5)$$

The integrated Brγ flux over the NLR is $\approx 4.2 \times 10^{-14}$ erg s^{-1} cm^{-2}. As discussed above, there is an average reddening of $E(B - V) = 0.5$ along the NLR. Correcting for this reddening, using the law of Cardelli et al. (1989) the Brγ flux is $F_{\rm Br\gamma} \approx 4.4 \times 10^{-14}$ erg s^{-1} cm^{-2}. Adopting an electronic density of 100 cm^3, we obtain $M_{\rm H\,II} \approx 2.4 \times 10^6\ {\rm M}_{\odot}$. The adopted density is justified by the fact that the resulting H II mass, divided by the volume of two cones with height of 100 pc and opening angle of 75° – the approximate geometry of the observed intensity distributions

– does result in a density value of ≈100 cm^{-3}. It may be that the density is higher, and the filling factor is smaller than 1, but the resulting mass will be the same.

We can also calculate the mass of hot H_2 (which emit the *K*-band emission lines) as in Riffel et al. (2008) and Scoville et al. (1982):

$$M_{H_2} = \frac{2 m_p \, F_{H_2\lambda 2.1218} \, 4\pi D^2}{f_{\nu=1,J=3} \, A_{S(1)} \, h\nu} = 5.0776 \times 10^{13} \left(\frac{F_{H_2\lambda 2.1218}}{\mathrm{erg\,s^{-1}\,cm^{-2}}}\right)\left(\frac{D}{\mathrm{Mpc}}\right)^2, \quad (6)$$

where m_p is the proton mass, $F_{H_2\lambda 2.1218}$ is the line flux, D is the distance to the galaxy and M_{H_2} is given in solar masses. For a typical vibrational temperature of $T_{vib} = 2000$ K (similar to the value we have obtained), the population fraction is $f_{\nu=1,J=3} = 1.22 \times 10^{-2}$ and the transition probability is $A_{S(1)} = 3.47 \times 10^{-7}\,s^{-1}$ (Turner, Kirby-Docken & Dalgarno 1977; Scoville et al. 1982; Riffel et al. 2008).

The total H_2 2.1218 flux, integrated over the whole emitting region, is 2.5×10^{-14} erg s^{-1} cm^{-2}. Correcting for the average reddening of $E(B - V) = 0.5$, we obtain $F_{H_2\lambda 2.1218} = 2.64 \times 10^{-14}$ erg s^{-1} cm^{-2}. Then, using the above expressions we obtain $M_{H_2} = 240\,M_\odot$.

This value is 10^4 times smaller than that of H II, but it should be noted that this mass is only of the hot H_2, which emits because either shocks (probably from the accretion flow along the bar) or X-rays from the AGN excite the H_2 molecule. Most of the molecular gas in the nuclear region of galaxies is cold, with the hot-to-cold mass ratio ranging between 10^{-7} and 10^{-5} (Dale et al. 2005). Thus, the total mass (hot plus cold) of molecular gas is probably even larger than that of H II. The presence of such a molecular gas reservoir around AGN is supported by radio observations of the central region of active galaxies, by, for example, the 'NUGA' group, which report molecular gas masses in the range 10^7–$10^9\,M_\odot$ in the inner a few hundred parsec of active galaxies (e.g. Garcia-Burillo et al. 2005; Boone et al. 2007; Krips et al. 2007). In the case of NGC 4151, as discussed above, Mundell & Shone (1999) have measured inflows in radio observations of H I along the large-scale bar (at PA 130°), which may be the origin of a molecular gas reservoir accumulated around the nucleus, only a small part of which we observe, due to excitation of the H_2 molecule.

5 SUMMARY AND CONCLUSIONS

We have mapped the emitting gas intensity distributions, reddening and excitation in the NLR of NGC 4151 using Gemini NIFS observations of the inner ≈200 × 300 pc^2 of the galaxy, covering the near-IR *Z, J, H* and *K* spectral bands, at a resolving power $R \geq 5000$ and spatial resolution of ≈8 pc. The main results of this paper are as follows.

(i) The intensity distributions in the recombination lines of H and He as well as in the [S III], [P II], [[Fe II] and [S III] emission lines, similarly to that in the optical [O III], are most extended along PA = 60/240° – the axis of the previously known bicone. The emitting region is somewhat brighter and reaches a larger projected distance of ≈130 pc from the nucleus to the SW (the near side of the bicone) than to the NE (the far side of the bicone), where it reaches a distance of ≈100 pc. The fluxes in the recombination lines decrease with distance r from the nucleus as $\propto r^{-1}$, while those on the other emission lines above remain constant or even increase with distance from the nucleus along the NLR.

(ii) The H_2 intensity distribution is completely different from that of the ionized gas, avoiding the region of the bicone, probably due to the destruction of the H_2 molecule by the strong ionizing flux along the bicone. Most of the H_2 emission seems to be coming not from the outflowing gas, but from gas which is in the plane of the galaxy. This is supported by its kinematics (Simões Lopes et al. in preparation). The concentration of the H_2 emission approximately perpendicular to the bicone indicates that there is attenuation of the ionizing flux at these locations, precluding the destruction of the H_2 molecule. This attenuation may be due to an obscuring torus and/or to the bottom part of the biconical outflow (as suggested by Kraemer et al. 2008).

(iii) The intensity distribution in the coronal line [Si VII] is resolved and that in the [Ca VIII] is marginally resolved, consistent with an origin in the inner NLR. The intensity distributions in these and the other coronal lines – [S VIII] and [S IX] – decrease steeply with distance as $\propto r^{-2}$, similarly to those of the calibration stars.

(iv) The line ratios [Fe II]λ1.257/1.644 and Paβ/Brγ were used to map the reddening along the NLR, which ranges from $E(B - V) = 0$ to 0.5. Within 0.5 arcsec from the nucleus, the reddening increases up to $E(B - V) \geq 1$.

(v) The [S III]/Pa β line ratio has a value of ≈11 to the SW (typical for the NLR of Seyfert galaxies), where we are looking at the inner wall of the near cone, and is ≈ 30 per cent lower to the NE, where we are looking at the outer wall of the far cone. This difference seems not to be due to reddening and indicates lower excitation to the NE.

(vi) The line-ratio map [Fe II] 1.257/[P II] 1.187 of the NGC 4151 NLR is the first such 2D map of an extragalactic source, and, similarly to the [Fe II] 1.257/Pa β ratio, shows larger values at the locations where the [Fe II] emission is enhanced at ≈1 arcsec from the nucleus. The increase in these line ratios maps the shocks produced by the radio jet in the NLR, which release the Fe II usually tied up in dust grains. This is confirmed by the correlation between the line-ratio maps and the outer parts of the radio map. From the many emission lines observed at the locations where the [Fe II] emission is enhanced, we have obtained the gas density, $N_e \approx 4000\,cm^{-3}$, and temperature $T_e \approx 15\,000 \pm 5000$ K.

(vii) From the fluxes of 10 H_2 emission lines, we have concluded that the H_2-emitting gas is in thermal equilibrium at the excitation temperature $T_{exc} = 2155$ K, ruling out any significant contribution from fluorescence to the excitation of the H_2 molecule. The thermal excitation may be due to X-rays from the AGN escaping perpendicular to the bicone axis or else to shocks produced by the accretion flow observed along the bar (Mundell et al. 1995) when the gas reaches the nuclear region.

(viii) We have calculated the mass of the ionized and molecular gas, obtaining for the former $M_{H\,II} \approx 2.4 \times 10^6\,M_\odot$ and for the latter only $M_{H_2} \approx 240\,M_\odot$. This small mass is nevertheless only that of the 'hot skin' of a probably much larger molecular gas mass.

(ix) The distinct intensity distribution and smaller temperature (as well as distinct kinematics; see Simões Lopes et al. in preparation) of the H_2 emission, when compared with those of the ionized gas, support a distinct origin for the emitting gas. The H_2 emission is probably a tracer of a large molecular gas reservoir, built up from the accretion flow observed along the large-scale bar, which may be the source of fuel to the AGN. The H_2 emission can thus be considered a tracer of the *feeding* of the AGN, while the ionized gas emission, which maps the outflowing gas, is a tracer of the *feedback* from the AGN.

ACKNOWLEDGMENTS

We thank an anonymous referee for his/her valuable suggestions which helped us to improve the paper, as well as Dr Irapuan Rodrigues for help with the IDL routine. Based on observations obtained at the Gemini Observatory, which is operated by the Association of Universities for Research in Astronomy, Inc., under a cooperative agreement with the NSF on behalf of the Gemini partnership: the National Science Foundation (United States), the Science and Technology Facilities Council (United Kingdom), the National Research Council (Canada), CONICYT (Chile), the Australian Research Council (Australia), Ministrio da Cincia e Tecnologia (Brazil) and Ministerio de Ciencia, Tecnología e Innovación Productiva (Argentina). This work has been partially supported by the Brazilian institution CNPq.

REFERENCES

Alexander T., Sturm E., Lutz D., Sternberg A., Netzer H., Genzel R., 1999, ApJ, 512, 204
Bautista M. A., Pradhan A. K., 1998, ApJ, 492, 650
Black J. H., van Dishoeck E. F., 1987, ApJ, 322, 412
Blietz M., Cameron M., Drapatz S., Genzel R., Krabbe A., van der Werf P., Sternberg A., Ward M., 1994, ApJ, 421, 92
Bohlin R. C., Savage B. D., Drake J. F., 1978, ApJ, 224, 132
Boone F. et al., 2007, A&A, 471, 113
Cappi M. et al., 2006, A&A, 446, 459
Cardelli J. A., Clayton G. C., Mathis J. S., 1989, ApJ, 345, 245
Crenshaw M., Kraemer S. B., 2005, ApJ, 625, 680
Crenshaw M., Kraemer S. B., 2007, ApJ, 659, 250
Crenshaw M. et al., 2000, AJ, 120, 1731
Dale D. A., Sheth K., Helou G., Regan M. W., Hüttemeister S., 2005, ApJ, 129, 2197
Das et al., 2005, AJ, 130, 945
Davies R. D., 1973, MNRAS, 161, 25P
Dopita M. A., Sutherland R. S., 1995, ApJ, 455, 468
Dopita M. A., Sutherland R. S., 1996, ApJS, 102, 161
Evans I. N., Tsvetanov Z., Kriss G. A., Ford H. C., Caganoff S., Koratkar A. P., 1993, ApJ, 417, 82
Fernandez B. R., Holloway A. J., Meaburn J., Pedlar A., Mundell C. G., 1999, MNRAS, 305, 319
Forbes D. A., Ward M. J., 1993, ApJ, 416, 150
Garcia-Burillo S., Combes F., Schinnerer E., Boone F., Hunt L. K., 2005, A&A, 441, 1011
Groves B. A., Dopita M. A., Sutherland R. S., 2004a, ApJS, 153, 9
Groves B. A., Dopita M. A., Sutherland R. S., 2004b, ApJS, 153, 75
Hollenbach D., McKee C. F., 1989, ApJ, 342, 306
Hutchings J. B. et al., 1998, ApJ, 492, L115
Hutchings J. B. et al., 1999, AJ, 118, 2101
Hutchings J. B., Crenshaw D. M., Kraemer S. B., Gabel J. R., Kaiser M. E., Weistrop D., Gull T. R., 2002, AJ, 124, 2543
Jackson N., Beswick R. J., 2007, MNRAS, 376, 719
Knop R. A., Armus L., Larkin J. E., Mathews K., Shupe D. L., Soifer B. T., 1996, AJ, 112, 81
Kraemer S. B., Crenshaw D. M., Hutchings J. B., Gull T. R., Kaiser M. E., Nelson C. H., Weistrop D., 2000, ApJ, 531, 278
Kraemer S. B. et al., 2001, ApJ, 551, 671
Kraemer S. B. et al., 2005, ApJ, 633, 693
Kraemer S. B. et al., 2006, ApJs, 167, 161
Kraemer S. B., Schmitt H. R., Crenshaw D. M., 2008, ApJ, 679, 1128
Krips M. et al., 2007, A&A, 468, L63
Kriss G. A., Davidsen A. F., Zheng W., Kruk J. W., Espey B. R., 1995, ApJ, 454, L7
Malkan M. A., 1983, ApJ, 264, L1
Maloney P. R., Hollembach D. J., Tielens A. G. G. M., 1996, ApJ, 466, 561
McGregor P. J. et al., 2003, in Iye M., Moorwood A. F. M., eds, Proc. SPIE Vol. 4841, Instrument Design and Performance for Optical/Infrared Ground-based Telescopes, SPIE, Bellingham, p. 1581
Mouri H., 1994, ApJ, 427, 777
Mouri H., Kawara K. & Taniguchi Y., 2000, ApJ, 528, 186
Mundell C. G., Shone D. L., 1999, MNRAS, 304, 475
Mundell C. G., Pedlar A., Shone L., Robinson A., 1999, MNRAS, 304, 481
Mundell C. G., Pedlar A., Baum S. A., O'Dea C. P., Gallimore J. F., Brinks E., 1995, MNRAS, 272, 355
Mundell C. G., Wrobel J. M., Pedlar A., Gallimore J., 2003, ApJ, 583, 192
Mediavilla E., Arribas S., 1995, MNRAS, 276, 579
Nussbaumer H., Storey P. J., 1988, A&A, 193, 327
Oliva E. et al., 2001, A&A, 369, L5
Osterbrock D. E., 1989, Astrophysics of Gaseous Nebulae and Active Galactic Nuclei. University Science Books, Mill Valley, California
Osterbrock D. E., Koski A. T., 1976, MNRAS, 176, 61P
Osterbrock D. E., Shaw R. A., Veilleux S., 1990, ApJ, 352, 561
Pedlar A., Howley P., Axon D., Unger S. W., 1992, MNRAS, 259, 369
Pedlar A., Kukula M. J., Longley D. P. T., Muxlow T. W. B., Axon D. J., Baum S., O'Dea C., Unger S. W., 1993, MNRAS, 263, 471
Penston M. V. et al., 1981, MNRAS, 196, 857
Prestwich A. H., Wright G. S., Joseph R. D., 1992, ApJS, 80, 205
Quinet P., Le Dourneuf M., Zeippen C. J., 1996, A&AS, 120, 361
Reunanen J., Kotilainen J. K., Prieto M., A., 2002, MNRAS, 331, 154
Rieke G. H., Lebofsky M. J., 1981, ApJ, 250, 87
Riffel R., Rodríguez-Ardila A., Pastoriza M. G., 2006a, A&A, 457, 61
Riffel R. A., Storchi-Bergmann T., Winge C., Barbosa F. K. B., 2006b, MNRAS, 373, 2
Riffel R. A., Storchi-Bergmann T., Winge C., McGregor P., Beck T., Schmitt H., 2008, MNRAS, 385, 1129
Rodriguez-Ardila A., Pastoriza M. G., Viegas S., Sigut T. A. A., Pradhan A. K., 2004, A&A, 425, 457
Rodriguez-Ardila A., Prieto M. A., Viegas S. M., Gruenwald R., 2006, ApJ, 653, 1098
Scoville N. Z., Hall D. N. B., Kleinmann S. G., Ridgway S. T., 1982, ApJ, 253, 136
Simpson C., Forbes D. A., Baker A. C., Ward M. J., 1996, MNRAS, 283, 777
Storchi-Bergmann T., Kinney A. L., Challis P., 1995, ApJS, 98, 103
Storchi-Bergmann T., Winge C., Ward M., Wilson A. S., 1999, MNRAS, 304, 35
Tompson R. I., 1995, ApJ, 445, 700
Turner J., Kirby-Docken K., Dalgarno A., 1977, ApJS, 35, 281
Turner J. E. H., Allington-Smith J., Chapman S., Content R., Done C., Haynes R., Lee D., Morris S., 2002, MNRAS, 331, 284
Ulrich M.-H., 2000, A&AR, 10, 135
Ward M. J., Geballe T., Smith M., Wade R., Williams P., 1987, ApJ, 316, 138
Weymann R. J., Morris S. L., Gray M. E., Hutchings J. B., 1997, ApJ, 483, 717
Wilman R. J., Edge A. C., Johnstone R. M., 2005, MNRAS, 359, 755
Winge C., Axon D. J., Macchetto F. D., Capetti A., 1997, ApJ, 487, L121
Zuther J., Iserlohe C., Pott J. U., Bertram T., Fischer S., Voges W., Hasinger G., Eckart A., 2007, A&A, 466, 451

This paper has been typeset from a TEX/LATEX file prepared by the author.